DOI: 10.1002/ejic.201000876

# Spin Crossover and Solvate Effects in 1D $Fe^{II}$ Chain Compounds Containing Bis(dipyridylamine)-Linked Triazine Ligands

**Tamsyn M. Ross,[a] Boujemaa Moubaraki,[a] David. R. Turner,[a] Gregory J. Halder,[b] Guillaume Chastanet,[c] Suzanne M. Neville,[c] John D. Cashion,[d] Jean-François Létard,[c] Stuart R. Batten,[a] and Keith S. Murray*[a]**

**Keywords:** Iron / Spin crossover / 1D coordination polymers / Magnetic properties / LIESST / Mössbauer effect / Solvates

A series of 1D polymeric $Fe^{II}$ spin crossover (SCO) compounds of type *trans*-$[Fe^{II}(NCX)_2(L)]$·Solvent has been synthesised {L = DPPyT = 1-[4,6-bis(dipyridin-2-ylamino)-1,3,5-triazin-2-yl]pyridin-4(1*H*)-one for **1**–**4**; NCX = $NCS^-$ for **1** and **2**, $NCSe^-$ for **3** and **4**; Solvent = $2.5CH_2Cl_2$ for **1**, $2CHCl_3$·$0.5CH_3OH$ for **2** and **4**, $CH_2Cl_2$ for **3**; L = DPT (6-phenoxy-$N^2$,$N^2$,$N^4$,$N^4$-tetra-2-pyridinyl-1,3,5-triazine-2,4-diamine) for **5**; NCX = $NCS^-$ for **5**; Solvent = $2CH_3OH$·$H_2O$ for **5**; L = DQT {4-[4,6-bis(dipyridin-2-ylamino)-1,3,5-triazin-2-yloxy]phenol} for **6**–**8**; $NCX^-$ = $NCS^-$ for **6**; Solvent = $2CH_2Cl_2$ for **6**; $NCX^-$ = $NCSe^-$ for **7**; Solvent = $CH_2Cl_2$·$CH_2ClCH_2Cl$ for **7**; $NCX^-$ = $NCSe^-$ for **8**; Solvent = $1.5CH_2Cl_2$·$0.5CH_3OH$ for **8**}. Two mononuclear complexes, *trans*-$[Fe^{II}(NCS)_2(DPT)_2]$·$2CH_3OH$ (**9**) and *trans*-$[Fe^{II}(NCSe)_2(DPT)_2]$·$2CH_3OH$ (**10**), contained the L ligand in a terminal bidentate coordination mode. As well as variations made in the $NCX^-$ ligands, variations were also made in substituent groups on the *s*-triazine "core" of L to investigate their intermolecular/supramolecular role in crystal packing and, thus, their influence on SCO properties. All the complexes crystallised as solvates, and the influence of the latter on the magnetism and spin transitions was explored. A wide range of physical methods was employed, as a function of temperature, viz. crystallography, PXRD (synchrotron), susceptibilities, LIESST and Mössbauer effect, in order to probe magnetostructural correlations in these 1D families. New examples of half-crossovers, with ordered –LS–HS–LS–HS– intrachain states existing below $T_{1/2}$, have been observed and comparisons made to related one- or two-step systems. All the observed transitions are gradual and non-hysteretic, and brief comments are made in relation to recent theoretical models for cooperativity, developed elsewhere.

## Introduction

The spin crossover (SCO) phenomenon involves spin state switching in some $d^4$–$d^7$ transition metals by external perturbations such as temperature, pressure or light irradiation.[1] Fundamental studies in this area have focused on, for example, the origins of cooperativity (the degree to which structural changes due to the spin transition are communicated throughout the crystal lattice, where high cooperativity results in an abrupt or hysteretic SCO). Polynuclear and polymeric species, particularly those that contain $Fe^{II}$ ($d^6$), have been the subject of much recent research[2] due to the possibility of synthesising multifunctional materials,[3] and the belief that covalent bridge-bonding between metal centres will enhance cooperativity.[4] Furthermore, second coordination sphere entities such as lattice solvent and non-coordinating anions, or intermolecular interactions such as hydrogen bonding,[5] may have a strong influence on the magnetic character and cooperativity of a particular compound by mediating interactions between SCO centres or affecting crystal packing (hence influencing "chemical pressure" within the crystal lattice), or by having an electronic influence on ligands.[6,7] Recent theoretical work by Robert et al. aimed at understanding thermal hysteresis in bistable, highly cooperative $[Fe(NCX)_2(bidentate)_2]$ monomers has provided new insights into how quantifiable electrostatic contributions control the hysteresis loop and how these change as the crystal structure changes along with the spin transition.[8,9] From a chemical perspective, particular recent interest has focused on host–guest capabilities in SCO materials, where further control over the magnetic character is possible.[10] One ultimate goal in spin switching chemistry is to achieve industrial applications,[11] and for instance, photomagnetic (LIESST; *L*ight *I*nduced *E*xcited *S*pin *S*tate *T*rapping) studies are conducted on SCO materials in the pursuit of room-temperature optical switches.[12]

[a] School of Chemistry, Building 23, Monash University, Clayton, Victoria 3800, Australia
Fax: +61-3-99054597
E-mail: keith.murray@monash.edu
[b] X-ray Science Division, Advanced Photon Source, Argonne National Laboratory, Argonne, Illinois 60439, USA
[c] CNRS, Université de Bordeaux, ICMCB, 87 avenue du Dr. A. Schweitzer, 33608 Pessac, France
[d] School of Physics, Monash University, Clayton, Victoria 3800, Australia
Supporting information for this article is available on the WWW under http://dx.doi.org/10.1002/ejic.201000876.

  

We recently reported the structure and magnetic properties of families of [4,6-bis(dipyridylamino)-3,4,5-triazine]-bridged and other 1D polymeric materials.[13,14] In the case, for example, of the compound *trans*-$[Fe^{II}(NCS)_2(cddt)]\cdot 2CH_3OH$ (polymorph **1c**)[13] [cddt = 2-chloro-4,6-bis(dipyrid-2-ylamino)-1,3,5-triazine] it displayed an incomplete two-step spin transition with a rare, ordered –HS–LS–HS–LS– chain structure at low temperatures. In contrast, another polymorph (**1b**) remained HS over all temperatures. Gamez and Reedijk et al.[15] have also reported dipyridylamino-substituted *s*-triazine bridged polynuclear $Fe^{II}$ crossover compounds, whereas Reedijk et al. discovered an intermediate phase, with ordered [HS–LS–HS] states, in a mononuclear *trans*-$[Fe^{II}(L')_2(NCS)_2]$ two-step SCO complex formed with a dipyridylamine/2,2′-bipyridine-type tetradentate ligand L′.[16]

In the present study we expand our library of 1D covalently bridged SCO materials containing [4,6-bis(dipyridylamine)-1,3,5-triazine]-type bridging ligands using the new ligands DPPyT {1-[4,6-bis(dipyridin-2-ylamino)-1,3,5-triazin-2-yl]pyridin-4(1*H*)-one}, DPT (6-phenoxy-$N^2$,$N^2$,$N^4$,$N^4$-tetra-2-pyridinyl-1,3,5-triazine-2,4-diamine) and DQT {4-[4,6-bis(dipyridin-2-ylamino)-1,3,5-triazin-2-yloxy]phenol}, as seen in Figure 1. There were a number of key aims in this study, all of a qualitative/phenomenological nature, and these were investigated by a comprehensive array of structural and magnetic methods. The first aim was to explore the intrachain effects of varying the ligand field around each $Fe^{II}$ atom generated by two $NCX^-$ ligands and two 2,2′-dipyridylamino (dpa) moieties of the adjacent, abovementioned bridging ligands L in complexes of type *trans*-$[Fe^{II}(NCX)_2(L)]$, where X = S and Se.

As well as the anticipated changes in $T_{1/2}$ arising, particularly from the $NCX^-$ variations (the ligand fields from the L ligands are expected to be similar), the variations in substituents in the 2-position of the triazine rings, shown in Figure 1, viz. a pyridone group (DPPyT), a phenoxy group (DPT) and a quinol-type group (DQT) were aimed at influencing crystal packing as well as providing possible H-bonding or π–π stacking between 1D chains that can often influence cooperativity.[5] Exploration of the influence on cooperativity and $T_{1/2}$ of these intermolecular interactions, along with other crystal-packing effects, such as $Fe^{II}$ first coordination sphere geometry, was of particular interest in the current study. Another question of importance was how common would be the earlier observation, in related ligand systems, of two-step spin transitions accompanied, or not, by ordered –LS–HS–LS–HS– states existing at the intermediate plateau temperature.[2,13,14] As the synthetic work proceeded, it became clear that crystals of the $Fe^{II}$ compounds were invariably solvated and thus, by synthesising and studying a range of such solvates, we sought to gain a better understanding of the manner in which second coordination sphere entities affect the magnetic character of these *trans*-$[Fe^{II}(NCX)_2(L)]\cdot$Solvent systems by a comparative structural study over a range of temperatures spanning the spin transition. Since the solvate molecules were often easily lost, great care was taken to ensure the samples measured were of the phase shown by crystallography and that desolvation had not occurred or, at least, was minimal. As indicated earlier, we are certainly not the first, or only group, to recognise solvate dependency in $Fe^{II}$ spin transitions, though there are relatively few such reports for 1D SCO materials. Some recent examples, by no means exhaustive, include single-crystal-to-single-crystal transformations induced by guest sorption/desorption, noted in mononuclear $Fe^{II}$ compounds by Oshio et al.[17] and Zheng et al.[18] and, in coordination-polymer SCO systems by Real et al.,[19] Kepert et al.[20] and Ohba and Kitagawa et al.[21] In a 1D $[Fe^{II}(Schiff\ base)(\mu\text{-}4,4'\text{-}bipyridine)]_n$ crystal, Weber et al. have observed solvent dependency of the spin transition concomitant with grinding of the crystals, whereas a precipitated powder sample of the same complex showed further differences.[22]

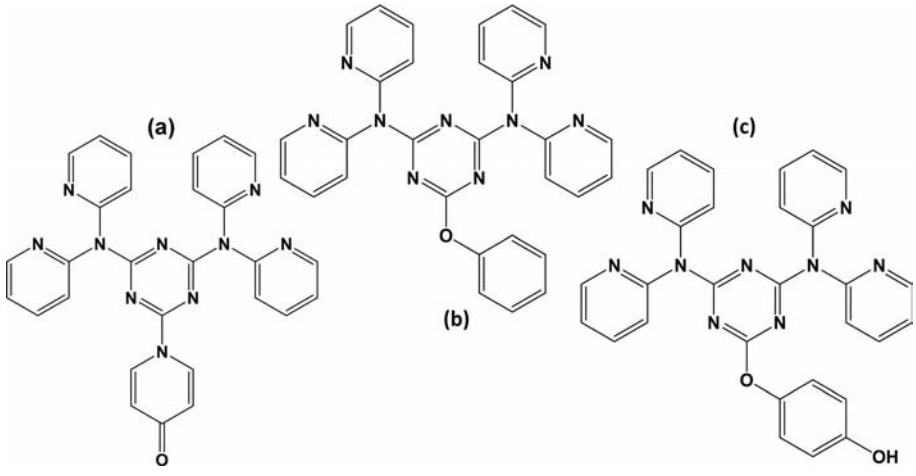


Figure 1. The ligands (a) DPPyT {1-[4,6-bis(dipyridin-2-ylamino)-1,3,5-triazin-2-yl]pyridin-4(1*H*)-one}, (b) DPT (6-phenoxy-$N^2$,$N^2$,$N^4$,$N^4$-tetra-2-pyridinyl-1,3,5-triazine-2,4-diamine) and (c) DQT {4-[4,6-bis(dipyridin-2-ylamino)-1,3,5-triazin-2-yloxy]phenol}.

  

## Results and Discussion

### Synthesis and Characterisation

The ligands DPPyT, DPT and DQT were synthesised by the reaction of cddt[23] with 4-hydroxypyridine, phenol or hydroquinone, respectively, in hot DMSO with *N*,*N*-diisopropylethylamine present as base. The yield for DQT was lower than those for the other two new ligands presented here. The $^{1}H$ and $^{13}C$ NMR spectra for these ligands are available in the Supporting Information, Figures S1–S6.

Syntheses of the $Fe^{II}$ 1D chain materials **1** {*trans*-[$Fe^{II}$(NCS)$_2$(DPPyT)]·2.5$CH_2Cl_2$}, **2** {*trans*-[$Fe^{II}$(NCS)$_2$(DPPyT)]·2$CHCl_3$·0.5$CH_3OH$}, **3** {*trans*-[$Fe^{II}$(NCSe)$_2$(DPPyT)]·$CH_2Cl_2$}, **4** {*trans*-[$Fe^{II}$(NCSe)$_2$(DPPyT)]·2$CHCl_3$·0.5$CH_3OH$}, **5** {*trans*-[$Fe^{II}$(NCS)$_2$(DPT)]·2$CH_3OH$·$H_2O$}, **6** {*trans*-[$Fe^{II}$(NCS)$_2$(DQT)]·2$CH_2Cl_2$}, **7** {*trans*-[$Fe^{II}$(NCSe)$_2$(DQT)]·$CH_2Cl_2$·$CH_2ClCH_2Cl$} and **8** {*trans*-[$Fe^{II}$(NCSe)$_2$(DQT)]·1.5$CH_2Cl_2$·0.5$CH_3OH$} were achieved by slow diffusion of the reagents Fe(NCX)$_2$ and L together in a reaction medium comprised usually of two solvents, but in some cases three solvents were used (see Experimental Section). In this manner, crystals suitable for single-crystal X-ray diffraction studies were grown for each of **1**, **2**, and **4**–**8**. Single-crystal X-ray diffraction studies revealed that each of these complexes is polymeric and consists of linear, 1D chains in which $Fe^{II}$ sites are chelated by the terminal pyridyl groups of the L ligands, the latter bridging between metal centres. The pyridyl moieties of L are chelated in equatorial positions around $Fe^{II}$ sites, and the $N_6$ coordination sphere at each $Fe^{II}$ site is completed by *trans*-axial $NCX^-$ ligands (for a more detailed discussion of the structural features, see the Structural Analysis section). A similar 1D structure is expected for **3**, although X-ray quality crystals were not produced.

Apart from compounds **9** and **10**, described below, the formation of $Fe^{II}$ coordination polymers was consistent here for all syntheses attempted. However, prediction of the constitution of the lattice solvent was not generally possible. The relative proportions of solvents present in the crystal lattices of **1**–**8** does not always reflect the relative proportions of these solvents present in the reaction media. To ensure accuracy of microanalytical and magnetic data, every effort was made to keep each product stored under the solvent that was found in its crystal lattice for as long as possible, prior to analysis, in order to minimise lattice solvent loss. Whereas it is acknowledged that, in some cases, some lattice solvent was lost quite quickly when products were removed from solvent, microanalytical data are, generally, in good agreement with calculated values. In the magnetism results we describe four samples of **1**, viz. **1**, $\mathbf{1}_{\alpha}$ (desolvated in air for 1 week), $\mathbf{1}_{\beta}$ (desolvated during transport to Bordeaux for photomagnetism), and $\mathbf{1}_{\gamma}$ (partial desolvation of a pristine sample that had been coated in grease prior to photomagnetic studies). Thus, these labels signify different degrees of solvation. Unfortunately, it was not possible to obtain any structural details for these partly or fully desolvated forms of **1** or of other desolvated complexes described here since they did not yield diffraction patterns. Microanalytical data were obtained on fully desolvated samples in some cases, such as $\mathbf{5}_{\alpha}$, and agreed with calculated values. The "parent" solvates **1**–**6** were each synthesised by using the described methods, reproducibly on more than one occasion, as judged by single-crystal X-ray studies. The parent solvate **7** was accessible by using two different concentrations of reactants (see Experimental Section and Supporting Information), whereas the parent solvate **8** was synthesised more than once by using the method described in the Experimental Section, as judged by single-crystal X-ray studies and microanalysis. The compounds **9** and **10**, synthesised by methods described in the Experimental Section, were each synthesised once only for the present study.

An interesting observation was that even though 1:1 ratios of Fe(NCX)$_2$/L were used in all cases involving the ligand DPT, mononuclear 1:2 products **9** {*trans*-[$Fe^{II}$(NCS)$_2$(DPT)$_2$]·2$CH_3OH$} and **10** {*trans*-[$Fe^{II}$(NCSe)$_2$(DPT)$_2$]·2$CH_3OH$} were crystallized when methanol was used both as diffusing solvent in the H-tubes employed for crystal growth, as well as the reaction medium for rapid precipitation of microcrystalline powder for bulk analysis.

### Magnetic Susceptibility and LIESST Studies

The magnetic and photomagnetic results for all compounds are given here, prior to their structural data, and discussions of magnetostructural and cooperativity correlations, relating to ligand and solvent variations, are given in the Discussion and Conclusion sections.

#### *trans-[$Fe^{II}$(NCX)$_2$(DPPyT)]·Solvent Series*

Complexes **1**–**4** all display gradual spin transitions with no thermal hysteresis noted when heating and cooling (see Figure 2). For **1**, the $\chi_M T$ value (per $Fe^{II}$ at 270 K in the high-spin (HS) plateau region) of 3.125 $cm^3 mol^{-1} K$ decreases gradually below 240 K, with $T_{1/2} \approx 175$ K. In the LS region, below ca. 120 K, the $\chi_M T$ values decrease slightly from ca. 0.5 $cm^3 mol^{-1} K$ to reach a minimum of 0.08 $cm^3 mol^{-1} K$ at 2 K. Such non-zero values of $\chi_M T$ below the spin transition are commonly observed[24] and are due to a combination of second-order Zeeman TIP (temperature-independent paramagnetic susceptibility) effects from the $t_{2g}^6$ $Fe^{II}$ centres and, perhaps, some remnant HS contribution. Figure 2(a) shows that the gradual spin transition for the desolvated (see above) sample $\mathbf{1}_{\alpha}$, has a slightly higher $T_{1/2}$ value of ca. 190 K, with a more conventional shape than that of **1** and with a higher low-spin (LS) plateau ($\chi_M T \approx 0.8$ $cm^3 mol^{-1} K$) than in the parent, indicative of a larger HS state contribution.

Mössbauer spectra were measured on selected examples of the present 1D families to confirm HS and LS states and complement the magnetic data. Complex **1** was measured at both room temperature (ca. 290 K) and 78 K (see Supporting Information, Figure S7). At room temperature the quadrupole splitting and isomer shift of 2.64(1) $mm s^{-1}$ and 1.05(1) $mm s^{-1}$, respectively, are typical of HS-state $Fe^{II}$.

  

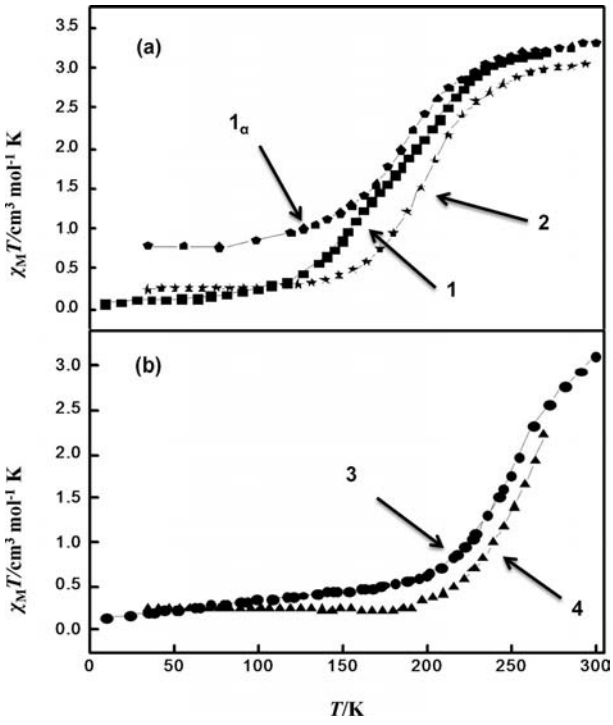


Figure 2. $\chi_M T$ plots for (a) **1** (filled squares), the desolvated sample $\mathbf{1}_{\alpha}$ (filled circles) and **2** (crosses), and (b) **3** (filled circles) and **4** (filled triangles).

The 78 K spectrum, corresponding to a predominantly LS state, shows a small residual HS doublet (ca. 8%), with a quadrupole splitting and isomer shift of 0.40 mm s$^{-1}$ and 0.51 mm s$^{-1}$ for the LS doublet, and 2.74(1) mm s$^{-1}$ and 1.46(1) mm s$^{-1}$ for the minor HS doublet. The fitting of the doublet due to the LS contribution (the main, narrow doublet) could not be carried out by using a simple one-Voigtian fit, which suggests that there are similar contributions from more than one species to this doublet. We suggest that the residual HS fraction and the possibility of more than one contributor to the LS doublet, may be due to a non-uniform, partial drying out of the sample despite efforts to retain full solvation.

In Figure 2(a) it can be seen that complex **2** shows a complete HS-to-LS transition, with $T_{1/2} \approx 200$ K, and an LS plateau value of $\chi_M T = 0.21$ cm$^3$ mol$^{-1}$ K. The plot of $\chi_M T$ for **3**, shows that the HS state has not been fully populated at 300 K, where $\chi_M T \approx 3.1$ cm$^3$ mol$^{-1}$ K [Figure 2(b)]. A full, gradual HS-to-LS transition is observed, with $T_{1/2} \approx 250$ K. The LS region, below ca. 200 K, shows $\chi_M T$ slowly decreasing, from ca. 0.5 cm$^3$ mol$^{-1}$ K at 200 K to ca. 0.2 cm$^3$ mol$^{-1}$ K at 4 K, likely indicative of some HS-state trapping at these low temperatures. The analogous chloroform/methanol solvate **4** likewise shows an incomplete crossover at 270 K [Figure 2(b)], with $T_{1/2}$ of ca. 260 K and with no hysteresis. The LS plateau has $\chi_M T \approx$ 0.2 cm$^3$ mol$^{-1}$ K. Thus, for both the $NCS^-$ and $NCSe^-$ analogues, with the higher $T_{1/2}$ being noted for $NCSe^-$ as expected, a higher value of $T_{1/2}$ was observed for the chloroform/methanol solvate compared to the dichloromethane solvate.

Photomagnetic LIESST (Light Induced Excited Spin State Trapping) studies were carried out on a desolvated sample of $\mathbf{1}_{\beta}$ [see Figure 3(a)]. The thermal susceptibility plot for $\mathbf{1}_{\beta}$ shows a full HS-to-LS transition that occurs in two slightly different stages. A $T_{1/2}$ of ca. 200 K is noted for $\mathbf{1}_{\beta}$, which is higher than that observed for **1** and $\mathbf{1}_{\alpha}$, and the shape of the spin transition is slightly different to that of $\mathbf{1}_{\alpha}$ possibly because of the different drying regimes used. The sample $\mathbf{1}_{\beta}$ was irradiated with green light (532 nm) at 10 K until photosaturation was achieved, resulting in ca. 40% trapping of a metastable HS state. The irradiation was then turned off and the sample heated, resulting in a rapid relaxation of the metastable HS state to the LS state by 70 K. The characteristic $T$(LIESST) value for this material is 30 K,[12] calculated by the minimum of $\delta\chi_M T/\delta T$, which relates to a location on the graph of $T_{(}$LIESST) vs. $T_{1/2}$ approximately along the $T_0 = 100$ K line.[12] This low value of $T$(LIESST) is in agreement with predictions that members of the $[Fe^{II}(L)_n(NCS)_2]$ family can be expected to have $T$(LIESST) values $< 125$ K.[25] The metastable HS state upon heating appears to be quite unstable, and this is prob-

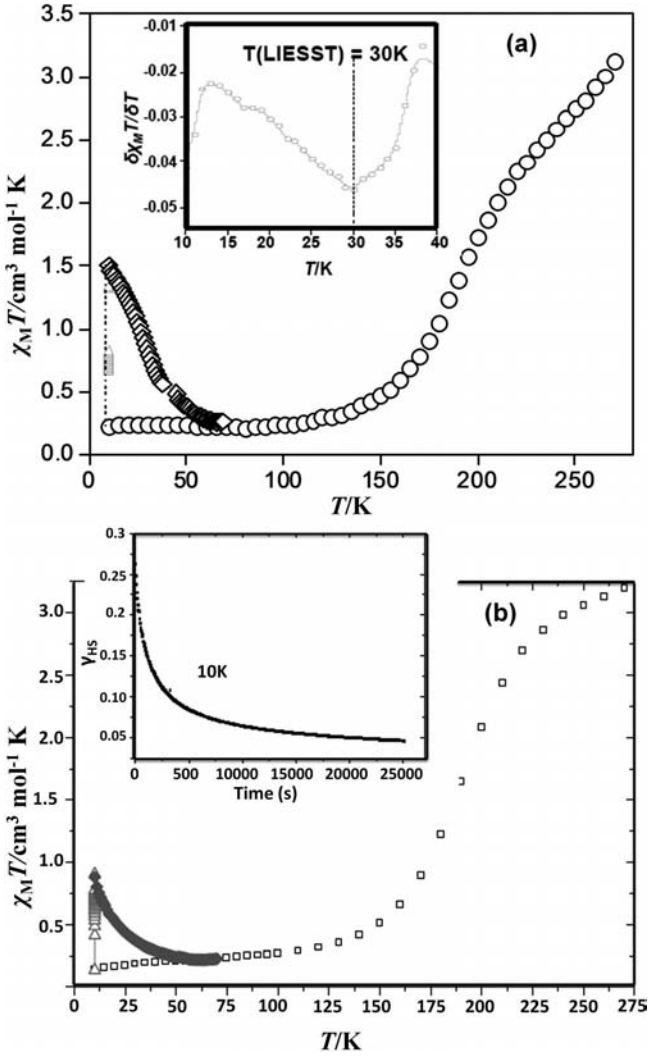


Figure 3. $\chi_M T$ plots and LIESST activity for (a) $\mathbf{1}_{\beta}$ and (b) $\mathbf{1}_{\gamma}$.

  

ably the reason for the incomplete HS trapping being observed here. Kinetics measurements were carried out on $\mathbf{1}_\beta$ at 10, 25, 32, 35, 38 and 40 K and show rapid relaxation of the trapped HS state even at 10 K by a stretched exponential behaviour (see Supporting Information, Figure S9). Fitting of the data yielded the parameters $E_A$ = 82 $cm^{-1}$, $k_{inf} = 2.5 \times 10^3$ $s^{-1}$, $\sigma$ = 28 $cm^{-1}$, with a very low activation energy indicative of little communication occurring in the lattice for the LIESST effect.

Attempts were also made to measure LIESST on a "fully solvated" sample of **1** ($\mathbf{1}_\gamma$; see above regarding the label) by carefully handling and purging at 200 K for a minimal time. However, on each occasion partial or full desolvation occurred. The $T_{1/2}$ value for $\mathbf{1}_\gamma$ of ca. 190 K [Figure 3(b)] does not match the $T_{1/2}$ value of ca. 175 K noted for the parent, fully solvated compound **1**, and it is suggested that the grease used to prevent desolvation was not sufficient to retain the dichloromethane molecules located in the crystal lattice. The grease-covered sample $\mathbf{1}_\gamma$ was cooled to 10 K, and then irradiated with green light (532 nm), and the sample warmed at a rate of 0.3 K $min^{-1}$. The magnetic susceptibility measurements on $\mathbf{1}_\gamma$ display a more conventional, continuous transition curve shape than both those of $\mathbf{1}_\beta$ and **1**. Unlike $\mathbf{1}_\alpha$, sample $\mathbf{1}_\gamma$ reaches a more complete transition from HS to LS at low temperatures. As **1**, $\mathbf{1}_\alpha$, $\mathbf{1}_\beta$, and $\mathbf{1}_\gamma$ all contain varying degrees of solvation, and display noticeably different temperature-dependent magnetic behaviour, this underscores the sensitivity of the magnetic character of these compounds towards the nature of the lattice solvation. The structural effects of loss or partial loss of lattice solvent could not be investigated here due to a simultaneous loss of crystallinity. Noticeable in Figure 3(b) is the low photo-excitation efficiency of $\mathbf{1}_\gamma$, as compared to $\mathbf{1}_\beta$. Due to the gradual nature of the LS-to-HS relaxation curve, no $T$(LIESST) could be determined. In addition to this, relaxation kinetics recorded at 10 K [insert, Figure 3(b)] suggest that $\mathbf{1}_\gamma$ is a fast-relaxing species with a lower activation-energy distribution than $\mathbf{1}_\beta$. The faster relaxation rate of $\mathbf{1}_\gamma$ may also be due to self-acceleration caused by a higher chemical pressure in $\mathbf{1}_\gamma$ that is not present in desolvated $\mathbf{1}_\beta$.

### *trans-[$Fe^{II}(NCX)_2(L)$]·Solvent Series where L = DPT and DQT*

The fully solvated parent complex **5** displays a continuous, incomplete SCO with $T_{1/2} \approx 190$ K. As can be seen in Figure 4(a), for **5** the $\chi_M T$ value per $Fe^{II}$ of ca. 3.4 $cm^3 mol^{-1} K$ at 250 K drops slightly until 210 K, where it has reached ca. 3.2 $cm^3 mol^{-1} K$. Between 210 K and 160 K $\chi_M T$ falls smoothly to ca. 1.6 $cm^3 mol^{-1} K$, indicating that a "half" SCO occurs. A portion of **5** was dried under high vacuum at 80 °C to remove lattice solvent, and magnetic susceptibility measurements were taken on the desolvated phase, labelled $\mathbf{5}_\alpha$. As seen in Figure 4(a), removal of solvent has caused not only a lowering of $T_{1/2}$ to ca. 165 K, but has resulted in a spin transition with a subtle two-step nature, the origin of which is not known. Between 300 K and 240 K, $\mathbf{5}_\alpha$ has a $\chi_M T$ value of ca. 3.4–3.3 $cm^3 mol^{-1} K$, which drops slowly between 240 K and 175 K to reach ca. 2.8 $cm^3 mol^{-1} K$. Below 175 K, the values drop off more rapidly until 140 K, at which point they tail off, reaching a low of $\chi_M T \approx 1.5$ $cm^3 mol^{-1} K$ at ca. 80 K. The small increase in magnetic moment at low temperatures is due to some thermal trapping of HS states (this is a common phe-

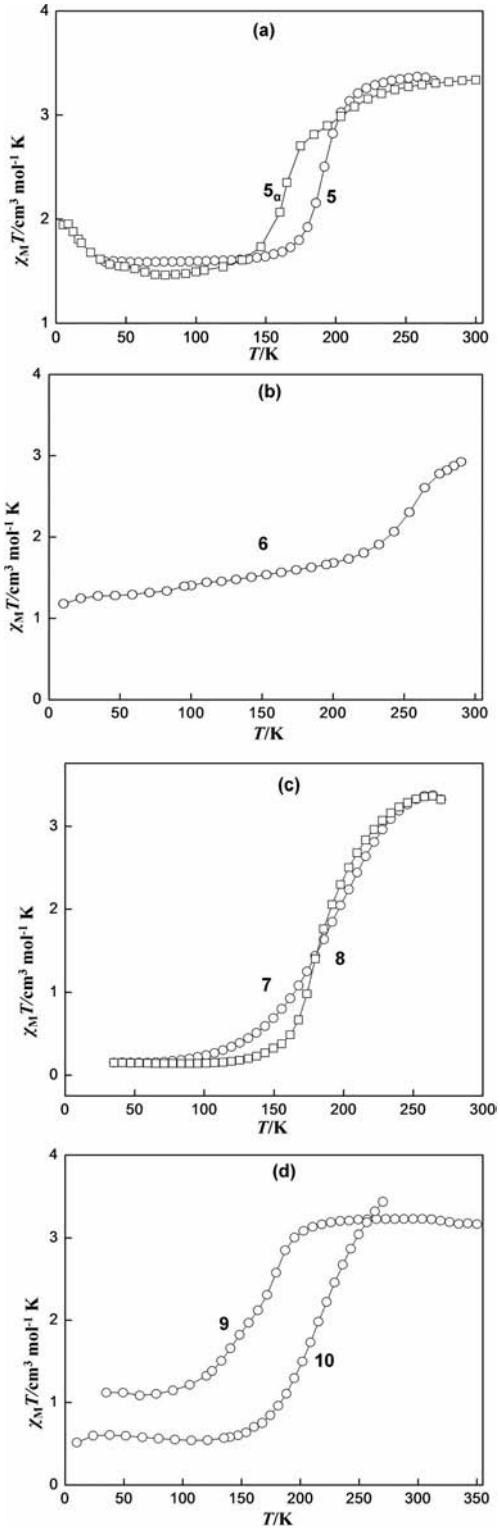


Figure 4. $\chi_M T$ plots for (a) **5** (open circles) and $\mathbf{5}_\alpha$ (open squares), (b) **6**, (c) **7** (open circles) and **8** (open squares), and (d) **9** and **10**.

  

nomenon when magnetic susceptibility measurements have been performed beginning at low temperatures, where the sample is quench-cooled to the lowest temperature, and magnetic susceptibility measurements taken as the temperature is raised. It was confirmed by cooling slowly while measuring). The incomplete SCO displayed by complex **6** contains several subtle steps and is significantly more gradual in nature than that of **5**. As seen in Figure 4(b), the $\chi_M T$ value for **6** is slightly smaller than ca. 3.0 $cm^3 mol^{-1} K$ at 290 K, indicating that at this temperature **6** is not fully HS and values drop slowly to reach ca. 2.7 $cm^3 mol^{-1} K$ at 260 K, whereupon a gentle step is observed. Below 260 K, the values drop more quickly until ca. 225 K, below which $\chi_M T$ decreases slowly to reach ca. 1.5 $cm^3 mol^{-1} K$ at 100 K. Below 100 K, there appears to be two subtle steps accompanying a slight decrease in $\chi_M T$ to ca. 1.1 $cm^3 mol^{-1} K$. The $T_{1/2}$ value of **6** is ca. 260 K.

Mössbauer effect measurements have been taken on **6** at room temperature (see Supporting Information) and at 78 K (Figure 5). The room-temperature spectrum (at ca. 298 K) shows a widely split doublet, fitted to a Lorentzian peak shape and attributed to HS $Fe^{II}$. The isomer shift and quadrupole splitting for this doublet are 1.04(1) $mm s^{-1}$ and 2.48(1) $mm s^{-1}$, respectively. The HS doublet accounts for ca. 95% of the recorded signal; however a small, narrow doublet with an isomer shift of 0.19(3) $mm s^{-1}$ and a quadrupole splitting of 0.50(6) $mm s^{-1}$ is noted to account for ca. 5% of the signal. This agrees with magnetic susceptibility measurements, which show that at 290 K **6** is not completely HS. The 78 K Mössbauer spectrum shows a contribution from HS $Fe^{II}$, and a narrow doublet due to a contribution from LS $Fe^{II}$. The HS and LS $Fe^{II}$ contributions each account for approximately 50% of the signal, and both the HS and LS doublets have been fitted by using a Voigtian peak shape as the lines showed a small deviation from the Lorentzian shape. For the HS doublet the isomer shift and quadrupole splitting are 1.17(1) $mm s^{-1}$ and 2.44(1) $mm s^{-1}$ respectively, and for the LS doublet the isomer shift and quadrupole splitting are 0.50(1) $mm s^{-1}$ and 0.32(1) $mm s^{-1}$ respectively.

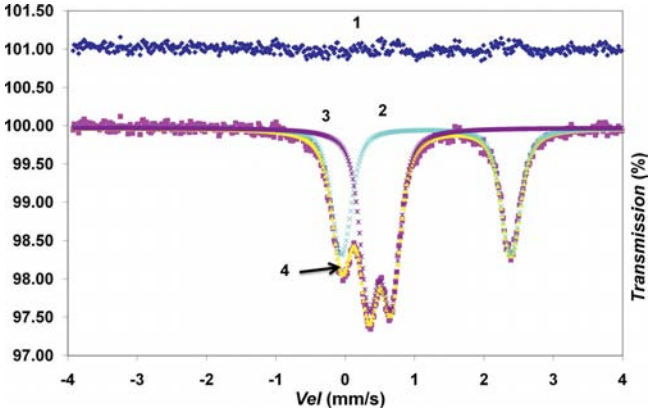


Figure 5. Mössbauer spectra (% transmission vs. velocity) taken on **6** at 78 K. Line 1 is the residual between the observed and fitted values, whereas line 2 is the best fit to the HS component, and line 3 is the best fit to the LS component. Line 4 (the most pale line) is the overall fit.

LIESST measurements were made on a fully solvated sample of **6**. As seen in Figure 6(a), only a low photoconversion was achieved. The characteristic $T$(LIESST) value,[12,25] as determined from the graph of $\delta\chi_M T/\delta T$ vs. $T$, is 52 K. This is higher than was observed for the desolvated sample of *trans*-$[Fe^{II}(NCS)_2(DPPyT)]\cdot 2.5CH_2Cl_2$ ($\mathbf{1}_\beta$) for which $T$(LIESST) was determined to be 30 K (vide supra). The $T$(LIESST) of 52 K, observed for **6**, relates closely to a location on the graph made by Létard et al. of $T$(LIESST) vs. $T_{1/2}$ along the $T_0$ = 120 K line.[12,25] As judged from the rapid decay of the metastable HS state with heating this state is quite unstable, and this is probably the reason for the incomplete HS trapping being observed for **6**. LIESST susceptibility measurements were also made on a sample of **5**.

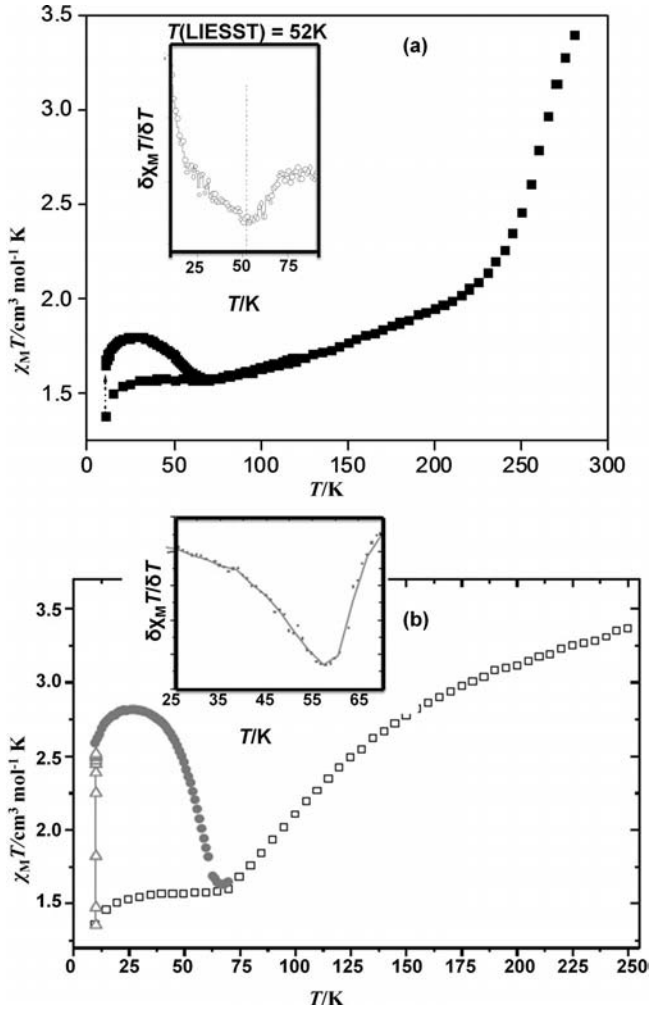


Figure 6. LIESST measurements made on (a) **6** and (b) $\mathbf{5}_\beta$.

Although great efforts were made to preserve the lattice methanol and water molecules in **5**, during the quick transfer of a sample of **5** into grease, some solvent loss seems to

  

have occurred. From the magnetic susceptibility curve shown in Figure 6(b), it is obvious that the relatively abrupt nature of the spin transition of the fully solvated complex **5** does not occur. It may also be noted that the magnetic susceptibility curve shown in Figure 6(b) does not match that of $\mathbf{5}_{\alpha}$, which was dried at 80 °C under high vacuum [see Figure 4(a)]. Thus, it would appear that a partially desolvated phase of **5**, denoted $\mathbf{5}_{\beta}$, has been used in the measurement of the LIESST effect. It is notable that $\mathbf{5}_{\beta}$ displays a significantly more gradual spin transition than $\mathbf{5}_{\alpha}$, the fully desolvated phase, and also shows a much lowered $T_{1/2}$ value (here, $T_{1/2} \approx 125$ K for $\mathbf{5}_{\beta}$). Sample $\mathbf{5}_{\beta}$, protected in grease, was cooled to 10 K, and then irradiated with green light (532 nm), and the sample warmed at a rate of 0.3 K $min^{-1}$. Figure 6(b) shows that ca. 80% photoconversion was achieved, much more than that seen for **6**, or for the complex *trans*-$[Fe^{II}(NCS)_2(DPPyT)]\cdot 2.5CH_2Cl_2$ (**1**), which showed ca. 40% photoconversion. The plot of $\delta\chi_M T/\delta T$ vs. $T$ indicates that $\mathbf{5}_{\beta}$ has a characteristic $T$(LIESST) of 58 K [see inset, Figure 6(b)]. Relaxation kinetics were measured for $\mathbf{5}_{\beta}$, and the relaxation rates were extracted by using a stretched exponential model. From this it was determined for $\mathbf{5}_{\beta}$ that $E_a = 585\ cm^{-1}$, $\sigma \approx 60\ cm^{-1}$, and $k_{\infty} = 2.6 \times 10^3\ s^{-1}$ (for details, see Supporting Information, Figure S10).

The magnetic data for the complexes **7** and **8** are plotted in Figure 4(c). Both fully solvated complexes have a $T_{1/2}$ value of ca. 175 K, and each shows a gradual, incomplete spin transition with a conventional shape and no stepwise nature. At 280 K, both **7** and **8** have a $\chi_M T$ value of ca. 3.5 $cm^3\,mol^{-1}\,K$; this value for **7** begins to decrease gradually at ca. 250 K, and reaches a low of ca. 0.2 $cm^3\,mol^{-1}\,K$ at 80 K. For **8**, the values begin to decrease at roughly the same temperature as for **7** (ca. 250 K); however, the spin transition is notably more abrupt for **8** than for **7**, where for **8** a low of ca. 0.2 $cm^3\,mol^{-1}\,K$ is reached at ca. 125 K. Surprisingly, these NCSe-bonded DQT compounds have a smaller $T_{1/2}$ value than does the NCS complex **6**.

The monomeric complexes **9** and **10** both show a gradual, incomplete spin transition. As seen in Figure 4(d), **9** has a $T_{1/2}$ value of ca. 150 K, whereas **10** has a $T_{1/2}$ value of ca. 210 K, as is expected due to the stronger ligand field generated by $NCSe^-$ (**10**) in comparison to that of $NCS^-$ (**9**). Between 300 K and 190 K, the $\chi_M T$ value of **9** is ca. 3.2 $cm^3\,mol^{-1}\,K$; above this temperature values fall slightly, possibly indicative of lattice methanol loss. Below 190 K the $\chi_M T$ of **9** decreases until ca. 90 K, at which point the lowest value of $\chi_M T \approx 1.1\ cm^3\,mol^{-1}\,K$ is reached, indicative of an incomplete SCO. The small increase below 90 K is due to HS thermal trapping. The magnetic susceptibility plot for **10** follows a more conventional shape for a gradual spin transition than does the 1D complex **6**. For **10**, a $\chi_M T$ value of ca. 3.5 $cm^3\,mol^{-1}\,K$ is noted at 280 K, and it decreases gradually from this point until 125 K, where a low of ca. 0.5 $cm^3\,mol^{-1}\,K$ is observed. It is suggested that incomplete relaxation to the LS state from HS thermal trapping may be the cause of the incomplete nature of the spin transition measured for **10**.

### Structural Analyses of 1D Complexes 1 {*trans*-$[Fe^{II}(NCS)_2(DPPyT)]\cdot 2.5CH_2Cl_2$}, 2 {*trans*-$[Fe^{II}(NCS)_2(DPPyT)]\cdot 2CHCl_3\cdot 0.5CH_3OH$}, 4 {*trans*-$[Fe^{II}(NCSe)_2(DPPyT)]\cdot 2CHCl_3\cdot 0.5CH_3OH$}, 5 {$[Fe^{II}(NCS)_2(DPT)]\cdot 2CH_3OH\cdot H_2O$}, 6 {*trans*-$[Fe^{II}(NCS)_2(DQT)]\cdot 2CH_2Cl_2$}, 7 {$[Fe^{II}(NCSe)_2(DQT)]\cdot CH_2Cl_2\cdot CH_2ClCH_2Cl$} and 8 {*trans*-$[Fe^{II}(NCSe)_2(DQT)]\cdot 1.5CH_2Cl_2\cdot 0.5CH_3OH$}

Crystallographic data were collected for the compounds **1**, **2** and **4** at three different temperatures spanning the spin transition of each compound (data for **1a** were collected at 100 K, for **1b** at 160 K, for **1c** at 250 K, for **2a** at 123 K, for **2b** at 200 K, for **2c** at 250 K, for **4a** at 100 K, for **4b** at 240 K, and for **4c** at 260 K). The structures of **1**, **2** and **4** are isotructural apart from the nature of the solvent. Their asymmetric units comprise one DPPyT ligand, two crystallographically distinct $Fe^{II}$ centres (Fe1 and Fe2, each on centres of inversion), each of which is chelated by a dpa moiety of DPPyT. There are also two crystallographically distinct $NCX^-$ ligands in the asymmetric units of **1**, **2** and **4**, each associated with one of the $Fe^{II}$ centres; NCX1 is coordinated to Fe1, and NCX2 is coordinated to Fe2. For **1**, the asymmetric unit also contains two and a half disordered dichloromethane molecules, whereas **2** and **4** contain two molecules of chloroform and one half-occupancy methanol molecule. A labelled representative example, with associated solvent omitted, appears in Figure 7. Complete asymmetric units for **1**, **2** and **4** may be viewed in the Supporting Information, Figures S11–S23.

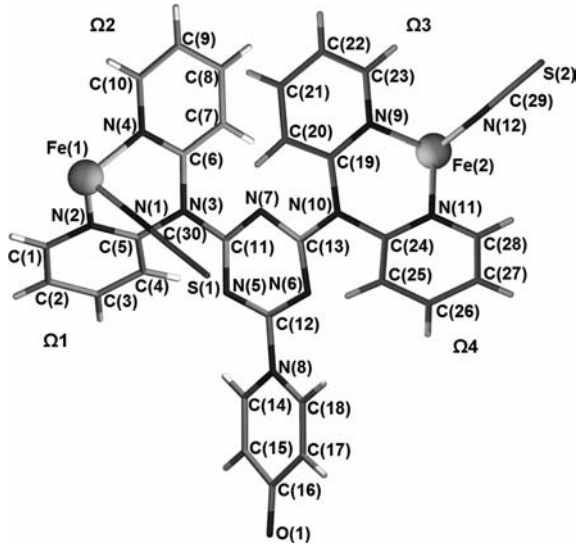


Figure 7. Asymmetric unit for **2** with solvent omitted, labelled with insignia relevant to the crystallographic discussion and tables in the Supporting Information.

Regarding the extended structures of **1**, **2** and **4**, the $N_6$ coordination environment of each $Fe^{II}$ centre is completed by two symmetry-equivalent axial *trans*-$NCX^-$ ligands and the chelating pyridyl groups of two symmetry-equivalent dpa moieties from two different DPPyT ligands, coordinated in equatorial fashion. In this manner, the structures

  

of **1**, **2** and **4** extend into linear 1D chains [Figure 8(a), see Tables 1, 2 and 3 for Fe···Fe distances], wherein each $Fe^{II}$ centre is linked to the next by a common DPPyT ligand, and each adjacent DPPyT ligand is rotated by 180°. The Fe1 and Fe2 centres alternate along these closely packed 1D chains [see Figure 8(b)]. The $NCX^-$ ligands extend into the spaces between the 1D chains, and S1···S2 or Se1···Se2 contacts between diagonally opposed 1D chains are present [**1a**: S···S 3.800(3) Å; **2a**: S···S 3.796(1) Å; **4a**: Se···Se 3.5885(6) Å; see Table S1 for these contacts in higher-temperature structures]. S···S contacts of lengths similar to those noted for **1** and **2** here have been previously reported for SCO materials.[26,27]

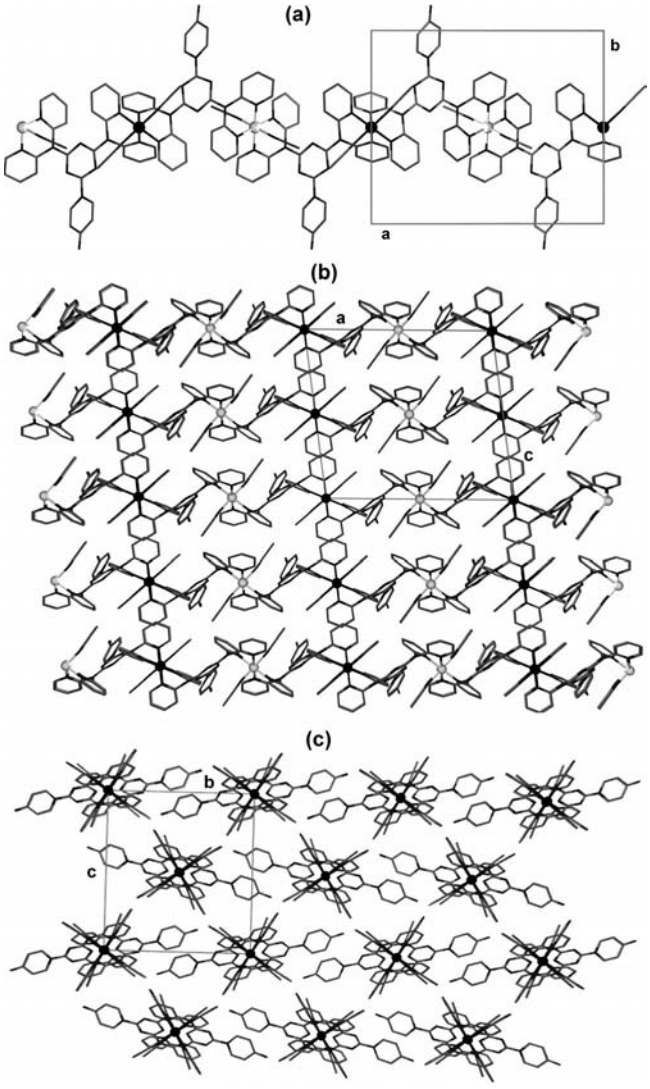


Figure 8. Packing diagrams representative of **1** {*trans*-$[Fe^{II}(NCS)_2$-$(DPPyT)]\cdot 2.5CH_2Cl_2$}, **2** {*trans*-$[Fe^{II}(NCS)_2(DPPyT)]\cdot 2CHCl_3\cdot 0.5CH_3OH$} and **4** {*trans*-$[Fe^{II}(NCSe)_2(DPPyT)]\cdot 2CHCl_3\cdot 0.5CH_3OH$}. Solvent molecules and hydrogen atoms have been omitted for clarity. (a) View along the *c*-axis, Fe1 and Fe2 sites are shown to alternate. (b) View along the *b*-axis showing the linear nature of the 1D chains. (c) View along the *a*-axis showing parallel packing of the 1D chains. In (a) and (b) Fe1 sites are shown as white spheres, and Fe2 sites are shown as black spheres.

Table 1. Interatomic parameters for **1**.

| | **1a** | **1b** | **1c** |
|---|---|---|---|
| *T* /K | 100 | 160 | 250 |
| Fe1–$N_{NCX}$ /Å | 1.958(6) | 1.962(5) | 2.078(8) |
| Fe2–$N_{NCX}$ /Å | 1.961(5) | 1.986(5) | 2.088(7) |
| Fe1–$N_{py}$ /Å | 1.998(6), 1.987(6) | 2.019(5), 2.009(5) | 2.198(7), 2.185(7) |
| Fe2–$N_{py}$ /Å | 1.983(5), 1.996(6) | 2.032(5), 2.033(6) | 2.192(7), 2.202(8) |
| Fe1–N–$C_{NCX}$ /° | 172.0(6) | 173.1(6) | 175.4(8) |
| Fe2–N–$C_{NCX}$ /° | 177.3(5) | 176.8(5) | 176.5(8) |
| ΣFe1°[a] | 29 | 32 | 41 |
| ΣFe2° | 26 | 31 | 39 |
| Φ1°[b] | 70 | 78 | 117 |
| Φ2° | 68 | 83 | 132 |
| Fe···$Fe_{intra}$ /Å[c] | 8.6913(4) | 8.7258(4) | 8.8290(2) |
| Fe···$Fe_{inter}$ /Å[d] | 10.5456(4) | 10.6006(3) | 10.8389(2) |
| X1···$cent_{triazine}$ /Å[e] | 3.54 | 3.54 | 3.57 |
| X2···$cent_{triazine}$ /Å | 3.31 | 3.34 | 3.44 |

[a] Σ° = sum of $|90 - \theta|$ for the 12 N–Fe–N angles in the octahedron.[25,28] [b] Φ° = sum of $|60 - \theta|$ for the 24 N–Fe–N angles describing the trigonal twist angle as described by Marchivie et al.[25] [c] Closest intrachain $Fe^{II}$–$Fe^{II}$ distance. [d] Closest interchain $Fe^{II}$–$Fe^{II}$ distance. [e] Distance from the S or Se atom to the centroid of the triazine ring of DPPyT.

Table 2. Interatomic parameters for **2**.

| | **2a** | **2b** | **2c** |
|---|---|---|---|
| *T* /K | 123 | 200 | 250 |
| Fe1–$N_{NCX}$ /Å | 1.958(3) | 2.052(7) | 2.092(8) |
| Fe2–$N_{NCX}$ /Å | 1.954(3) | 1.981(7) | 2.084(8) |
| Fe1–$N_{py}$ /Å | 2.010(3), 1.991(3) | 2.145(7), 2.110(7) | 2.220(7), 2.166(8) |
| Fe2–$N_{py}$ /Å | 1.987(3), 2.002(3) | 2.006(7), 2.033(6) | 2.156(7), 2.197(8) |
| Fe1–N–$C_{NCX}$ /° | 171.0(3) | 169.7(7) | 171.0(8) |
| Fe2–N–$C_{NCX}$ /° | 177.5(3) | 178.5(7) | 177.0(9) |
| ΣFe1°[a] | 33 | 39 | 42 |
| ΣFe2° | 27 | 31 | 40 |
| Φ1°[b] | 78 | 105 | 119 |
| Φ2° | 69 | 80 | 117 |
| Fe···$Fe_{intra}$ /Å[c] | 8.6794(4) | 8.6942(7) | 8.7806(6) |
| Fe···$Fe_{inter}$ /Å[d] | 10.6409(3) | 10.7507(6) | 10.8612(6) |
| X1···$cent_{triazine}$ /Å[e] | 3.62 | 3.69 | 3.70 |
| X2···$cent_{triazine}$ /Å | 3.34 | 3.39 | 3.45 |

[a] Σ° = sum of $|90 - \theta|$ for the 12 N–Fe–N angles in the octahedron.[25,28] [b] Φ° = sum of $|60 - \theta|$ for the 24 N–Fe–N angles describing the trigonal twist angle as described by Marchivie et al.[25] [c] Closest intrachain $Fe^{II}$–$Fe^{II}$ distance. [d] Closest interchain $Fe^{II}$–$Fe^{II}$ distance. [e] Distance from the S or Se atom to the centroid of the triazine ring of DPPyT.

Tables 1, 2 and 3 contain Fe–N bond lengths for **1**, **2** and **4** at each temperature investigated. Typically, HS $Fe^{II}$ bond lengths are ca. 2.0–2.1 Å for Fe–$N_{NCS}$ and ca. 2.1–2.4 Å for Fe–$N_{py}$, with a difference of ca. 0.2 Å in Fe–$N_{py}$ noted between HS and LS values (a smaller difference is observed for Fe–$N_{NCS}$).[28]

For **1c** and **2c**, Fe–N distances are consistent with those expected for HS $Fe^{II}$, whereas in **4c** Fe–N distances show a generally admixed HS/LS character, in accordance with magnetic susceptibility measurements, which show that **4** is not completely HS at 260 K. **1a**, **2a** and **4a** show typical LS

  

Table 3. Interatomic parameters for **4**.

| | **4a** | **4b** | **4c** |
|---|---|---|---|
| $T$ /K | 100 | 240 | 260 |
| Fe1–$N_{NCX}$ /Å | 1.948(3) | 2.007(4) | 2.048(5) |
| Fe2–$N_{NCX}$ /Å | 1.946(4) | 1.963(4) | 1.992(5) |
| Fe1–$N_{py}$ /Å | 2.004(3), 1.984(3) | 2.085(4), 2.060(4) | 2.140(5), 2.109(5) |
| Fe2–$N_{py}$ /Å | 1.980(3), 1.993(3) | 2.010(4), 2.016(4) | 2.052(5), 2.069(5) |
| Fe1–N–$C_{NCX}$ /° | 169.8(3) | 170.3(4) | 170.3(5) |
| Fe2–N–$C_{NCX}$ /° | 177.6(3) | 177.2(4) | 177.0(5) |
| ΣFe1°[a] | 34 | 38 | 41 |
| ΣFe2° | 29 | 30 | 34 |
| Φ1°[b] | 78 | 96 | 108 |
| Φ2° | 74 | 79 | 92 |
| Fe···$Fe_{intra}$ /Å[c] | 8.7029(6) | 8.736(1) | 8.7527(2) |
| Fe···$Fe_{inter}$ /Å[d] | 10.6978(5) | 10.843(1) | 10.8992(2) |
| X1···$cent_{triazine}$ /Å[e] | 3.76 | 3.80 | 3.83 |
| X2···$cent_{triazine}$ /Å | 3.42 | 3.47 | 3.50 |

[a] Σ° = sum of $|90 - \theta|$ for the 12 N–Fe–N angles in the octahedron.[25,28] [b] Φ° = sum of $|60 - \theta|$ for the 24 N–Fe–N angles describing the trigonal twist angle as described by Marchivie et al.[25] [c] Closest intrachain $Fe^{II}$–$Fe^{II}$ distance. [d] Closest interchain $Fe^{II}$–$Fe^{II}$ distance. [e] Distance from the S or Se atom to the centroid of the triazine ring of DPPyT.

$Fe^{II}$ Fe–N bond lengths. Mid-range temperature structural data show that whereas the Fe1 and Fe2 centres in **1b** have Fe–$N_{py}$ and Fe–$N_{NCS}$ distances that are not significantly different to each other (both showing admixed HS/LS character), in **2b**, **4b** and **4c** Fe1 has significantly more HS character than does Fe2. This suggests that for **1** both unique $Fe^{II}$ centres undergo a simultaneous spin transition, whereas in **2** and **4** the spin transition for Fe1 and Fe2 is slightly staggered (i.e. Fe1 and Fe2 have slightly different $T_{1/2}$ values). A transposition of the asymmetric units of **2a** and **2c** is shown in Figure 9, where small movements of the pyridyl moieties of DPPyT resulting from Fe–N bond length contractions are seen.

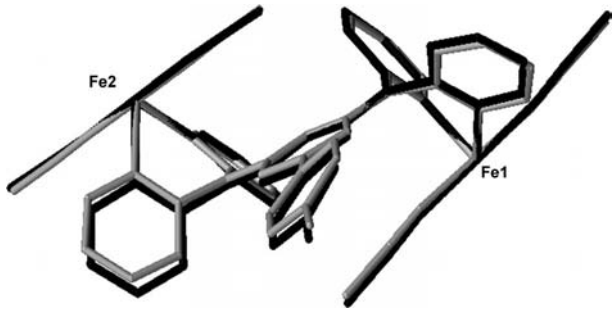


Figure 9. Transposition of the asymmetric units of **2a** (grey wire) and **2c** (black wire) with view along the *b*-axis. Hydrogen atoms and solvent molecules have been omitted for clarity.

Changes in the unit-cell parameters are observed over the spin transition (Tables 7, 8 and 9). With decreasing temperature, **1** displays an overall contraction of the magnitude of *a* and *c* and the angle *β*, accompanied by an overall increase of that in *b*. For **2** and **4** a comparatively small, overall contraction is noted for *a* and *c* and the angle *β*, and *b* decreases as the temperature decreases. Other differences between the solvates include the magnitudes of the Σ° and Φ° parameters (see Tables 1, 2 and 3).

The crystal structures of compounds **5** and **6** are generally similar and are described together. Crystal data were collected at a range of temperatures (100 K for **5a** and **6a**, 190 K for **5b** and 250 K for **6b**) such that the structure of each compound in an LS state, in a mid-range or a predominantly HS state was determined. For both **5** and **6**, the asymmetric unit consists of one DPT or DQT ligand, respectively, coordinated equatorially to two unique $Fe^{II}$ centres (Fe1 and Fe2, both on centres of inversion) by the terminal, chelating dpa substituents of the relevant bridging ligand. Each $Fe^{II}$ centre is coordinated, in an axial position, by one unique $NCS^-$ ligand, viz. NCS1$^-$ and NCS2$^-$ for Fe1 and Fe2, respectively. For **5**, two molecules of methanol and one molecule of water occur per asymmetric unit, and for **6** two molecules of dichloromethane occur per asymmetric unit. The asymmetric units of **5a** and **5b** are identical, as are the asymmetric units of **6a** and **6b**.

Figure 10(a) displays the asymmetric unit for **6**, with lattice solvent omitted, and labelled with Greek symbols, Ω1–5, relevant to discussion given later here, and tables in the Supporting Information. The symbols shown in Figure 10(a) are also applicable to **5**, as DPT and DQT ligands have been labelled identically in each crystal structure, with the exception of the hydroxy group located on the quinol moiety of DQT, which does not appear in DPT, henceforth referred to as $O_{quinol}$. Figures of complete asymmetric units for all structures are located in the Supporting Information (Figures S24–S34).

The extended structures of **5** and **6** consist of parallel-packed, infinite, linear 1D chains, wherein each $Fe^{II}$ centre has an $[Fe^{II}(NCS)_2(py)_4]$ coordination environment. Figure 10(b) and (c) show the manner in which Fe1 and Fe2 centres alternate along an individual 1D chain. S···S interactions between NCS2$^-$ ligands within adjacent 1D chains, as well as facial π-stacking interactions between Ω5 moieties in adjacent 1D chains, are shown in Figure 10(c) (these are discussed further below). The disparity between the unique $Fe^{II}$ centres in both **5** and **6**, Fe1 and Fe2, is evident in the Fe–N bond lengths (Table 4). At all temperatures, for both **5** and **6**, the Fe2–N distances are in good agreement with expected values for HS $Fe^{II}$, whereas Fe1–N distances are consistent with LS $Fe^{II}$ in **5a** and **6a**, and increase with increasing temperature.[28] This suggests that while a spin transition is occurring at Fe1 sites in both **5** and **6**, Fe2 sites remain HS over all temperatures. Magnetic susceptibility measurements on **5** and **6**, described above, indicate a "half" SCO in each case, in agreement with these observations of Fe–N bond lengths.

The crystal structures of the complexes **7** and **8** were both determined at 100 K (**7a** and **8a**) and 250 K (**7b** and **8b**), and are generally similar. For neither **7** nor **8** was a crystallographic phase change noted to accompany the spin transition. In each case the asymmetric unit consists of two unique $Fe^{II}$ centres, each on a centre of inversion and each

  

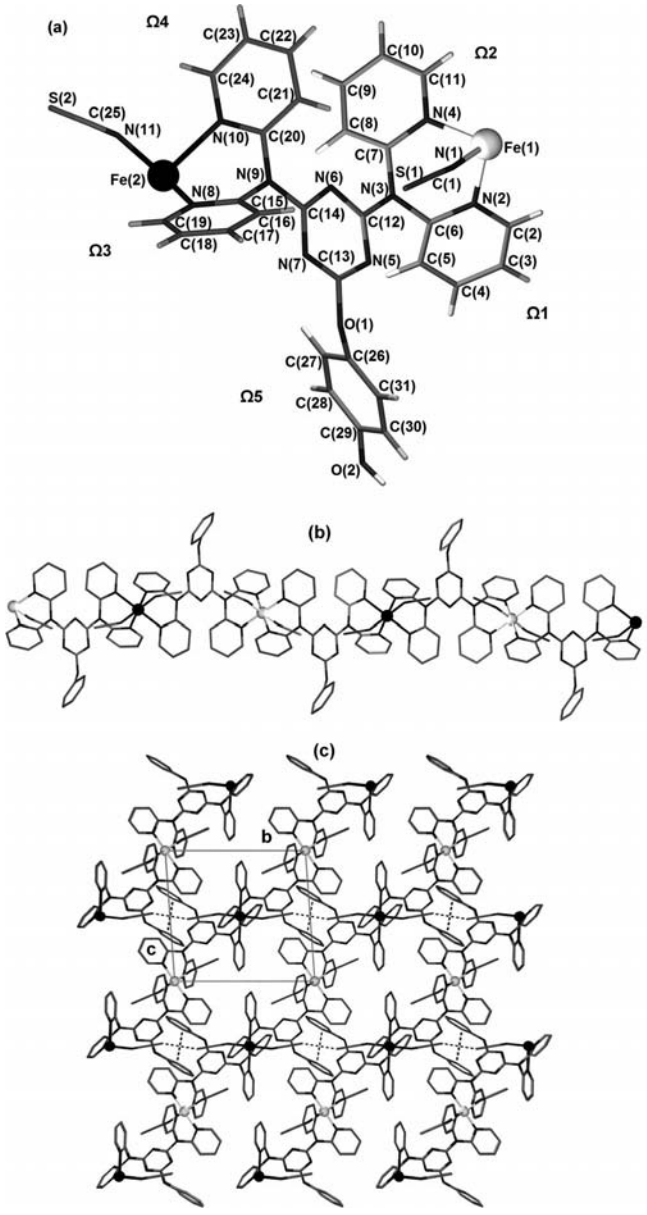


Figure 10. (a) Labeled asymmetric unit for **6a**, (b) single 1D chain of **5a** showing alternating Fe1 and Fe2 sites, and (c) packing diagram for **5a**, with view along the *a*-axis, showing S···S and face-to-face π-stacking interactions between Ω5 moieties. Hydrogen atoms and lattice solvent molecules have been omitted for clarity, and Fe1 atoms are shown as white spheres, whereas Fe2 atoms are shown as black spheres.

Table 4. Interatomic parameters for **5**, **6**.

| | **5a** | **5b** | **6a** | **6b** |
|---|---|---|---|---|
| *T* /K | 100 | 190 | 100 | 250 |
| Fe1–$N_{NCX}$ /Å | 1.951(3) | 2.062(3) | 1.949(4) | 2.000(5) |
| Fe2–$N_{NCX}$ /Å | 2.056(3) | 2.053(3) | 2.060(4) | 2.061(5) |
| Fe1–$N_{py}$ /Å | 1.988(3), 1.988(3) | 2.135(4), 2.130(3) | 1.999(4), 1.981(4) | 2.070(5), 2.060(6) |
| Fe2–$N_{py}$ /Å | 2.254(3), 2.244(3) | 2.258(3), 2.244(3) | 2.269(4) 2.256(4) | 2.277(7), 2.256(5) |
| Fe1–N–$C_{NCX}$ /° | 168.7(3) | 166.5(3) | 172.1(4) | 172.9(4) |
| Fe2–N–$C_{NCX}$ /° | 158.2(3) | 159.7(3) | 162.1(4) | 162.3(5) |
| ΣFe1°[a] | 29 | 37 | 30 | 34 |
| ΣFe2° | 43 | 44 | 46 | 49 |
| Φ1°[b] | 81 | 110 | 79 | 82 |
| Φ2° | 138 | 147 | 159 | 155 |
| Fe1···$Fe2_{intra}$ /Å | 9.187(1) | 9.280(2) | 9.212(2) | 9.273(9) |
| Fe···$Fe_{inter}$ /Å | 9.576(1) | 9.748(2) | 9.585(2) | 9.755(8) |
| X1···X1 /Å | – | – | – | – |
| X2···X2 /Å | 3.219(2) | 3.247(2) | 3.269(2) | 3.375(3) |
| X1···$cent_{triazine}$ /Å[c] | 3.60 | 3.71 | 3.59 | 3.63 |
| X2···$cent_{triazine}$ /Å | 3.58 | 3.58 | 3.53 | 3.58 |

[a] Σ° = sum of $|90 - \theta|$ for the 12 N–Fe–N angles in the octahedron.[25,28] [b] Φ° = sum of $|60 - \theta|$ for the 24 N–Fe–N angles describing the trigonal twist angle.[25] [c] Distance from the S or Se atom to the centroid of the triazine ring of DPT or DQT.

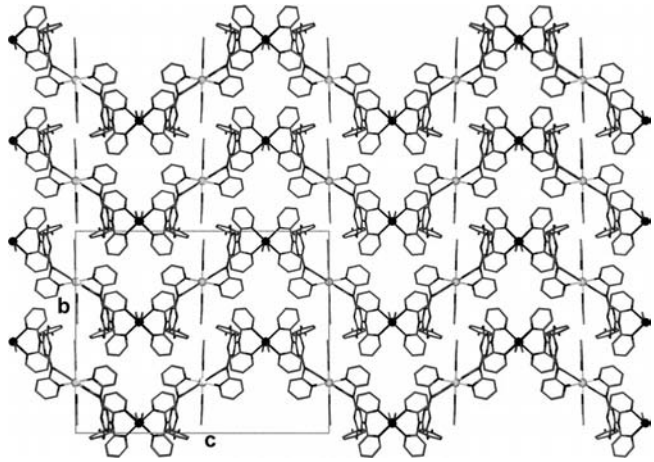


Figure 11. Packing diagram of **7a** with view along the *a*-axis. Solvent and hydrogen atoms have been omitted for clarity. Fe1 atoms are shown as white spheres, and Fe2 atoms are shown as black spheres.

bound equatorially to the terminal, chelating pyridyl groups of a DQT ligand. Bound to each unique $Fe^{II}$ centre in the asymmetric units of **7** and **8** is a unique $NCSe^-$ ligand ($NCSe1^-$ for Fe1 and $NCSe2^-$ for Fe2), coordinated in axial position, similar to that seen for **5** and **6**. The structures of **7** and **8** consist of zig-zag 1D chains, in which each Fe2 centre in a particular 1D chain constitutes a turning point in the direction of propagation (see Figure 11). In each zig-zag 1D chain, Fe1 and Fe2 centres alternate, and, notably, within each chain the $NCSe1^-$ and $NCSe2^-$ ligands are oriented in quite different directions.

Within the extended structures of **7** and **8** all zig-zag 1D chains run parallel, and are closely packed (see Figure 11). In both **7** and **8** lattice solvent molecules sit between the chains in very similar locations. In **7b** and **8b** (at 250 K) Fe–$N_{py}$ and Fe–$N_{NCS}$ distances indicate that Fe2 is in the HS state, whereas for Fe1 the Fe–$N_{NCS}$ distances are slightly shorter than those observed for Fe2 and indicate a small LS contribution (Table 5). There is no difference between the Fe–N bond lengths in **7b** and those in **8b**. At 100 K, Fe–N distances in **8a** indicate that both Fe1 and Fe2 are LS; however, whereas in **7a** Fe1 appears to be in an LS

  

state, the Fe2–$N_{py}$ bond lengths indicate that Fe2 has some residual HS character. It must be noted that the difference between the Fe2–$N_{py}$ bond lengths in **7a** and **8a** is very small. The disparity in spin states between Fe1 and Fe2 sites in both **7a** and **7b** clearly indicates slightly different $T_{1/2}$ values for Fe1 and Fe2, as has been seen previously in other SCO materials.[18] The disparity in the Fe–$N_{NCS}$ bond lengths between Fe1 and Fe2 in **8b**, as discussed above, suggests that Fe1 and Fe2 in **8** also have slightly different $T_{1/2}$ values, although the spin transitions of both Fe1 and Fe2 are complete at 100 K.

Table 5. Interatomic parameters for **7**, **8**.

| | **7a** | **7b** | **8a** | **8b** |
|---|---|---|---|---|
| *T* /K | 100 | 250 | 100 | 250 |
| Fe1–$N_{NCX}$ /Å | 1.930(8) | 2.044(8) | 1.927(7) | 2.036(7) |
| Fe2–$N_{NCX}$ /Å | 2.000(8) | 2.113(7) | 1.975(7) | 2.117(7) |
| Fe1–$N_{py}$ /Å | 2.001(7), 2.002(7) | 2.189(8), 2.160(7) | 2.002(6), 2.000(6) | 2.190(7), 2.170(7) |
| Fe2–$N_{py}$ /Å | 2.067(9), 2.061(8) | 2.209(7), 2.214(7) | 2.014(7), 2.013(7) | 2.200(7), 2.208(7) |
| Fe1–N–$C_{NCX}$ /° | 176.9(7) | 177.7(7) | 177.4(7) | 178.9(7) |
| Fe2–N–$C_{NCX}$ /° | 163.1(9) | 159.2(9) | 165.7(8) | 159.4(9) |
| ΣFe1°[a] | 28 | 40 | 26 | 40 |
| ΣFe2° | 36 | 48 | 34 | 46 |
| Φ1°[b] | 78 | 141 | 79 | 139 |
| Φ2° | 94 | 132 | 89 | 137 |
| Fe1···$Fe2_{intra}$ /Å | 9.012(2) | 9.131(1) | 8.982(2) | 9.130(4) |
| Fe···$Fe_{inter}$ /Å | 9.723(3) | 9.843(2) | 9.703(3) | 9.847(2) |
| X1···X1 /Å | 3.253(2) | 3.378(2) | 3.222(2) | 3.376(2) |
| X2···X2 /Å | 3.417(2) | 3.479(2) | 3.400(2) | 3.477(3) |
| X1···$cent_{triazine}$ /Å[c] | 3.43 | 3.49 | 3.43 | 3.48 |
| X2···$cent_{triazine}$ /Å | 3.54 | 3.64 | 3.51 | 3.65 |

[a] Σ° = sum of $|90 - \theta|$ for the 12 N–Fe–N angles in the octahedron.[25,28] [b] Φ° = sum of $|60 - \theta|$ for the 24 N–Fe–N angles describing the trigonal twist angle.[25] [c] Distance from the S or Se atom to the centroid of the triazine ring of DPT or DQT.

### Variable-Temperature Synchrotron Powder X-ray Diffraction and Single-Crystal X-ray Diffraction of *trans*-$[Fe^{II}(NCS)_2(DPPyT)]\cdot 2CHCl_3\cdot 0.5CH_3OH$ (2) and *trans*-$[Fe^{II}(NCS)_2(DQT)]\cdot 2CH_2Cl_2$ (6)

Variable-temperature powder X-ray diffraction (VTPXRD) was carried out on samples of **2** and **6** by using synchrotron radiation. This was done to provide a complementary method to susceptibilities for probing the gradual spin transitions observed. Care was taken to ensure that no loss of solvent occurred while microcrystalline samples were loaded into capillaries. Details of why samples **2** and **6** were measured, and not others, are given in the Supporting Information, the chief reason being the relative stability of the solvated forms, with attempts to measure other examples proving unsuccessful. Powder diffraction data were collected as indicated in the Exp. Sect. The lattice parameters at each temperature were determined from a single Le Bail fit to the data.[29] Full details of unit-cell parameters are located in the Supporting Information along with representative diffraction images. No crystallographic phase change was noted for **2** or **6** over the temperature range investigated.

Such VTPXRD studies have previously been reported for a number of SCO compounds, including *trans*-$[Fe^{II}(NCS)_2(cddt)]\cdot 2CH_3OH$ (polymorph **1c**), allowing insight into the dynamic behaviour of these materials on a molecular level as the spin transition occurs.[13,30] Anisotropy is expected in the temperature-dependent behaviour of the unit-cell parameters,[28] and changes in any one parameter are generally non-linear. The curve described by the unit-cell volume of **2** as temperature decreases strongly resembles the magnetic susceptibility plot (see Supporting Information, Figure S36). A total contraction of ca. 5.5% of the HS volume (taken as the volume at 250 K) is observed over the temperature range 250–100 K. Previous studies have shown that a total unit-cell volume contraction of ca. 2% may be attributed to the spin transition, where the remainder of the unit-cell contraction is due to isotropic thermal effects.[31]

For **2**, the temperature-dependent behaviour of *c* is similar to that observed for the unit-cell volume, where a smooth, gradual contraction of ca. 4% is noted to occur over the course of the spin transition. Figure 12(a) shows the temperature-dependent behaviour of *a* and *b* and the angle *β* for **2**, each given as a proportion of its value at 250 K. The curve describing the evolution of *b* shows two subtle points of inflection (one at ca. 225 K and one at ca. 200 K), whereas *a* and the angle *β* each show a rapid contraction within the region of 250–200 K; below 200 K each parameter continues to contract, but at a decreased rate. The fluctuations in the length of *b* are suggestive of complex dynamic phenomena in the solid-state arrangement of **2** as it undergoes the spin transition. That the majority of the change in *a* and the angle *β*, along with the two inflection points in the length of *b*, are all localised within the region of 250–200 K, suggests that the behaviour of these lattice parameters may be interrelated. To probe the nature of this relationship, and hence the nature of the internal phenomena occurring within **2** during the spin transition, full structural data collected on single crystals of **2** were examined.

By comparing the structure of **2c** to that of **2b** (Table 2) changes occurring as the temperature decreases from 250 to 200 K may be identified. As mentioned previously, these include a change in Fe–N bond lengths for both Fe1 and Fe2, where a greater contraction is noted at the Fe2 site, and also differences in Σ° and Φ° at both metal centres. Fe···Fe distances also decrease between **2b** and **2c**. In order to further probe the influence of structural rearrangements on the temperature-dependent behaviour of *b*, full structural data have been obtained at 260 K (**2d**), 250 K (**2e**), 230 K (**2f**) and 220 K (**2g**) (see Supporting Information for full crystallographic and structural details). It was anticipated that marked structural differences would be noted between **2g** at 220 K (the first point of inflection at which the length of *b* begins to increase with decreasing temperature) and **2b** at 200 K (the second point of inflection at which *b* begins once more to decrease with decreas-

  

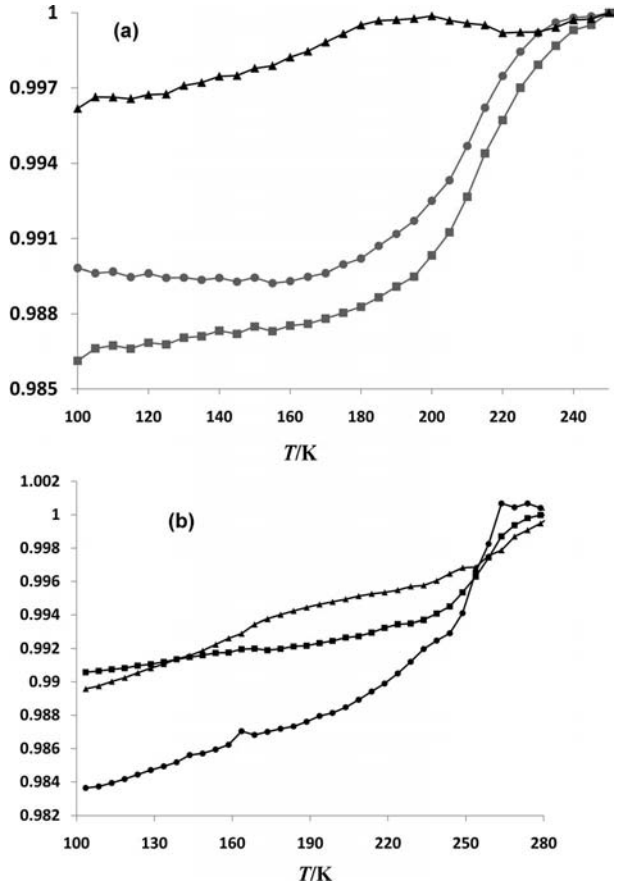


Figure 12. (a) Temperature-dependent PXRD behaviour for **2** of *a* (filled grey squares), *b* (filled black triangles) and the angle *β* (filled grey circles). Each parameter is given as a proportion of its value at 250 K; (b) temperature-dependent PXRD behaviour for **6** of *a*, *b* and *c*, where the value of each axis is given as a proportion of its value at 280 K. Here, *a* is shown as filled circles, *b* is shown as filled squares, and *c* is shown as filled triangles.

ing temperature). In general, it is noted that investigated parameters in **2f** and **2g** are intermediate to values determined for **2c** and **2b**, with only small differences observed in several parameters between **2g** and **2b**, including Fe2–$N_{py}$ and Fe2–$N_{NCX}$, but not Fe1–$N_{py}$ or Fe1–$N_{NCX}$ (see Tables 1, 2 and 3 and Figures S14–S20 in the Supporting Information). It is proposed that structural rearrangements occurring within the region 220–200 K, likely to involve primarily movement around the Fe2 site, may result in a rate of expansion in the direction of the *b*-axis larger than the rate of contraction due to the Fe–N bond shortening or thermal effects.

No crystallographic phase changes were noted for **6** over the temperature range investigated. Full details and pictures of all unit cell parameters are provided in the Supporting Information, Table S9 and Figures S37–S39. The shape of the curve described by the temperature-dependent behaviour of the unit-cell volume is very similar to that obtained during magnetic susceptibility measurements on **6**, which is a common feature in these types of studies.[13,32] A total volume change of ca. 4.7% is observed for **6**, which is considerably larger than that noted for *trans*-[$Fe^{II}(NCS)_2$(cddt)]·$2CH_3OH$ (polymorph **1c**),[13] that showed a volume change of ca. 3.5% for this "half"-SCO compound. In contrast, for **2**, which displays a more complete SCO than **6**, a total volume change of ca. 5.5% was observed. Figure 12(b) shows the changes in the *a*, *b* and *c* unit-cell parameters with changing temperature for **6**, which crystallises in the triclinic space group $P\bar{1}$. Pronounced non-linearity was also observed in the angles *α*, *β* and *γ* (see Supporting Information, Figure S39).

From Figure 12(b) it can be seen that in the temperature region 270–240 K *a* and *b* show an increased rate of change. A corresponding increased rate of change in each of the angles *α*, *β* and *γ* is noted within the same temperature region, suggesting that the behaviour of these parameters are related i.e. due to the same phenomenon occurring on a molecular level. It has long been known that intermolecular interactions can modulate the temperature-dependent behaviour of the unit-cell parameters.[33] As seen in Figure 12(b), *a* decreases by a larger proportion of its HS (280 K) length than do *b* or *c*. It is suspected that the close S···S interactions occurring parallel to the *b*-axis direction, and the face-to-face π-stacking occurring between Ω5 moieties on adjacent 1D chains related by symmetry by one unit-cell length translation in the direction of the *c*-axis [see Figure 10(c)] may restrict the amount by which *b* and *c* may contract.

### Structural Analysis of Mononuclear Compound 10 {*trans*-$[Fe^{II}(NCS)_2(DPT)_2]\cdot 2CH_3OH$}

The crystal structure of **10** has been determined at 100 K (**10a**), 200 K (**10b**) and 250 K (**10c**). No crystallographic phase transitions are observed for **10**. The structure of **10** consists of monomeric units in which an $Fe^{II}$ centre is coordinated by two axial $NCS^-$ ligands, and the Ω1 and Ω2 moieties of two DPT ligands. The Ω3 and Ω4 moieties of each DPT ligand remain uncoordinated, but participate in aryl interactions (see Table S6). Crystallographic refinement details are located in Table 12, and complete, labeled asymmetric units for each of **10a**, **10b** and **10c** are in Figures S28–S30. The Fe–$N_{NCS}$ and Fe–$N_{py}$ bond lengths in **10a** are consistent with expected values for LS $Fe^{II}$ species

Table 6. Interatomic parameters for **10**.

| | **10b** | **10a** | **10b** |
|---|---|---|---|
| *T* /K | 100 | 200 | 250 |
| Fe1–$N_{NCX}$ /Å | 1.945(4) | 1.975(4) | 2.046(5) |
| Fe1–$N_{py}$ /Å | 1.993(4), 1.992(4) | 2.039(4), 2.038(4) | 2.145(5), 2.140(5) |
| Fe1–N–$C_{NCX}$ /° | 171.0(4) | 171.6(4) | 172.2(5) |
| ΣFe1°[a] | 30 | 32 | 37 |
| Φ1°[b] | 77 | 87 | 113 |
| Fe···$Fe_{inter}$ /Å | 8.799(5) | 8.859(3) | 8.95(1) |
| X1···$cent_{triazine}$ /Å[c] | 3.73 | 3.77 | 3.83 |

[a] Σ° = sum of $|90 - \theta|$ for the 12 N–Fe–N angles in the octahedron.[25,28] [b] Φ° = sum of $|60 - \theta|$ for the 24 N–Fe–N angles describing the trigonal twist angle.[25] [c] Distance from the S or Se atom to the centroid of the triazine ring of DPT or DQT.

  

(ca. 1.96 Å), as seen in Table 6, whereas in **10b** and **10c** they are longer indicating an admixed HS/LS character where the relevant bond lengths for **10c** have more HS character than those for **10b**. This is in agreement with magnetic susceptibility measurements. A number of aryl interactions are noted to occur between monomeric units (see Table S6). The gradual nature of the spin transition observed for **10** indicates that these aromatic interactions result in little cooperativity.

## Discussion

All of the new 1D complexes described here display gradual spin transitions, as measured by susceptibilities and VTPXRD, and without any thermal hysteresis. Though some of the transitions are more abrupt than others, this behavior is generally indicative of weak cooperativity occurring. The various factors that affect the magnetism are now discussed.

### Structure–Magnetism Relations

#### *(i) Intrachain and $Fe^{II}$ Coordination Sphere Features*

Each of **1**, **2** and **4** displays a gradual spin transition (Figure 2) in agreement with previous findings suggesting that flexible linkers between $Fe^{II}$ centres, such as those afforded by DPPyT, are ineffective in communicating changes due to the spin transition.[34] Between the $NCS^-$ analogues, **1** displays a slightly more gradual transition than **2**, despite possible lag effects resulting from the differing transition temperatures of Fe1 and Fe2 in **2**. The distortion of the $FeN_6$ octahedron has been linked to both $T_{1/2}$ and the abruptness of a spin transition; for instance larger values of Φ° at HS have been linked to more abrupt transitions, whereas a larger ΔΦ° value between HS and LS for a particular metal centre has been linked to a lower value of $T_{1/2}$.[25] Here, a generally smaller value of ΔΦ° is noted for **2**, and this compound does display a higher $T_{1/2}$ value than **1**; however, **1** has generally larger values of Φ° at HS than **2**, but displays a less abrupt spin transition. It is suggested that differences in the abruptness of the spin transition between **1** and **2** are likely contributed to by all of the subtle disparities between the solvates, as discussed further below.

The linear 1D chain complexes **5** and **6** provide new examples, within this dpa-substituted *s*-triazine bridged series, of half-crossovers with ordered –LS–HS–LS–HS– states, being observed by crystallography at temperatures below the spin transition. Other examples have been reviewed, both of the half crossover type, such as *trans*-$[Fe^{II}(NCS)_2(cddt)]\cdot 2CH_3OH$ (polymorph **1c**),[13] and of the two-step SCO type, the latter showing ordered spin states at the intermediate plateau.[2] It is difficult to unambiguously identify both within the present DPT and DQT examples and by comparison to others studied,[13,14] why this ordering (trapping) of states occurs. One common feature is that most of these 1D compounds show two structurally different $Fe^{II}$ sites, albeit slightly. In **5** and **6**, a spin transition is occurring at the Fe1 sites (vide supra), whereas Fe2 sites remain HS over all temperatures. We did not observe diffuse scattering in the diffraction patterns of any of the present 1D complexes, as was the case in *trans*-$[Fe(NCSe)_2(bdpp)]$, where bdpp = 4,6-bis(2′,2′′-dipyridylamino)pyrimidine,[14] that had an averaged LS/HS character at the intermediate plateau between the two steps of the spin transition. In that compound, 1D ordering of alternating LS/HS $Fe^{II}$ centres occurred along the 1D chains but not between chains, and onset of the ordering was probably electronically driven.

In the zig-zag chain complexes **7** and **8**, the structurally distinct $Fe^{II}$ sites again occur. Looking in some detail at these compounds, both **7** and **8** undergo a continuous, full-spin transition with $T_{1/2} \approx 175$ K, where the spin transition for **7** is more gradual than that observed for **8** (Figure 4). The gradual nature of the spin transitions noted for both **7** and **8** is attributed to poor communication between inequivalent $Fe^{II}$ centres. It has already been established that incorporating flexible organic linkers into polymeric SCO systems is unlikely to improve cooperativity, and although cooperative interactions are possible by Se···Se interactions, discussed below, these occur only between equivalent $Fe^{II}$ centres within **7** and **8**. Thus, although cooperative interactions are possible between equivalent $Fe^{II}$ centres, differences in $T_{1/2}$ between Fe1 and Fe2 likely contribute to the gradual nature of the spin transition observed on the bulk. The crystal structures of **7** and **8** are remarkably similar, and there are few notable differences. In the comparison of **7a** to **8a** differences in structural parameters cannot be identified as either inherent or due to the inequivalence of spin states. Thus, between **7b** and **8b**, where **7** and **8** are in equivalent stages of the spin transition, as judged by the Fe–N bond lengths, differences in the various parameters listed in Tables 5, 11 and S7 are limited to: Φ° at both $Fe^{II}$ centres, ΣFe2°, Se1···$centroid_{triazine}$ and Se2···$centroid_{triazine}$, and the length of the unit-cell parameter *b*. It has been noted in discussing the DPPyT examples that distortions of the $FeN_6$ octahedron can affect both the $T_{1/2}$ value and the abruptness of a spin transition, and that larger values of Φ° in the HS state correlate to a more abrupt spin transition.[25,28] Differences in the $FeN_6$ octahedron distortions between **7** and **8** are, however, quite small. It is suggested that the subtle packing differences between these solvates, in combination with the influence on ligand electronics of the different solvation modes, culminate in a larger difference in $T_{1/2}$ between Fe1 and Fe2 in **7** than in **8**, causing a larger "lag" effect observed in bulk magnetic susceptibility measurements.

#### *(ii) Intermolecular and Inter-Chain Effects, Including Solvent H-Bonding Interactions*

We begin by discussing interactions involving the non-bonded sulfur atoms of the $NCS^-$ ligands in the DPT-and DQT-bridged species **5** and **6**. Table 4 contains a number of bond lengths, angles and close contacts relevant to the NCS1$^-$ and NCS2$^-$ ligands. It is notable that for both **5** and **6**, NCS1$^-$ and NCS2$^-$ participate in S···π interactions

  

between the electron-rich S atom of the $NCS^-$ ligands and the electron-deficient s-triazine ring of DPT or DQT.[35] As can be seen in Figure 10(c), the NCS2⁻ ligands are positioned such that they participate in S···S interactions between adjacent chains related by one unit-cell length translation in the *b*-axis direction (see Table 4). Such close S···S contacts between $NCS^-$ ligands have been noted previously in SCO compounds.[26] Although packing diagrams are for **5a**, the situation is analogous for the structures **5b**, **6a** and **6b**. An S···O interaction is noted in **6** between NCS1⁻ and $O_{quinol}$ on adjacent chains generated by symmetry by one unit-cell length translation in the direction of the *a*-axis [**6a**: S1···$O_{quinol}$ 3.275(4) Å]. It is also noted that Ω5 substituents of both DPT and DQT in **5** and **6**, respectively, engage in an apparent slipped face-to-face π-stacking interaction between adjacent 1D chains related by symmetry by one unit-cell length translation in the direction of the *c*-axis [in **5a** the closest C···C distance is 3.285(7) Å, with a centroid–centroid separation of 5.30 Å, and in **6a** the closest C···C distance is 3.18(1) Å, with a centroid–centroid separation of 5.06 Å]. These slipped π-stacking interactions form a solvent-free "pocket", isolating NCS2⁻ ligands from areas where lattice solvent is located [Figure 10 (c)] for **5**.

Whereas the NCS2⁻ ligands are largely isolated from lattice solvent in solvent-free pockets, NCS1⁻ ligands point directly into solvent-filled pockets between 1D chains. Figure 13(a) shows a packing diagram for **5**, with solvent molecules included. As illustrated in Figure 13(b) the solvent in **5** forms a localised hydrogen-bonding network. The network consists of a central six-membered $(H_2O)_2(CH_3OH)_4$ ring, and the water molecules of this ring also hydrogen-bond to the S atoms of NCS1⁻ ligands on adjoining chains. Thus, adjacent chains are connected through the intercalated hydrogen-bonding solvent. The S···O and O···O distances relevant to this H-bonding network for **5a** are S1···O4 3.214(4), O4···O2 2.847(5), O4···O3 2.734(6), O2···O3 2.755(5) Å. The analogous pocket in **6** also contains solvent molecules, in this case four dichloromethane molecules.

Superficially, the arrangement of the solvent molecules looks similar to that of **5**, as shown in Figure 13(c); however, there are only four solvent molecules present, not six, and the closest contacts between the solvent molecules and the $NCS^-$ anions are more consistent with van der Waals contacts than with the significant hydrogen bonding seen in **5**. The contact distances shown in Figure 13(c) for **6a** are S1···Cl1 3.494(2), Cl4···H32B 2.883, S1···H33B 2.835 Å. Whereas the contact distances within the $(H_2O)_2(CH_3OH)_4$ localised hydrogen-bonding network in **5** do not change between **5a** to **5b**, the contact distances in the van der Waals contacts between the lattice dichloromethane molecules and $NCS^-$ ligands in **6** become larger between **6a** and **6b** (see Table S5 in the Supporting Information).

It is suggested that the localised $(H_2O)_2(CH_3OH)_4$ hydrogen-bonding network in **5** provides the imperative for the small Fe1–N–$C_{NCX}$° change noted to occur between **5a** and **5b**, where no such change in Fe1–N–$C_{NCX}$° is observed for **6**. It is thought that the $(H_2O)_2(CH_3OH)_4$ hydrogen-bonding network in **5** is more effective for communication of changes due to the spin transition than the van der Waals contacts involving dichloromethane molecules in **6**, and this contributes to the more abrupt nature of the spin transition observed for **5** in comparison to that seen for **6**. Other subtle differences between **5** and **6**, as explored above, may also contribute to differences between the spin transitions observed for these compounds.

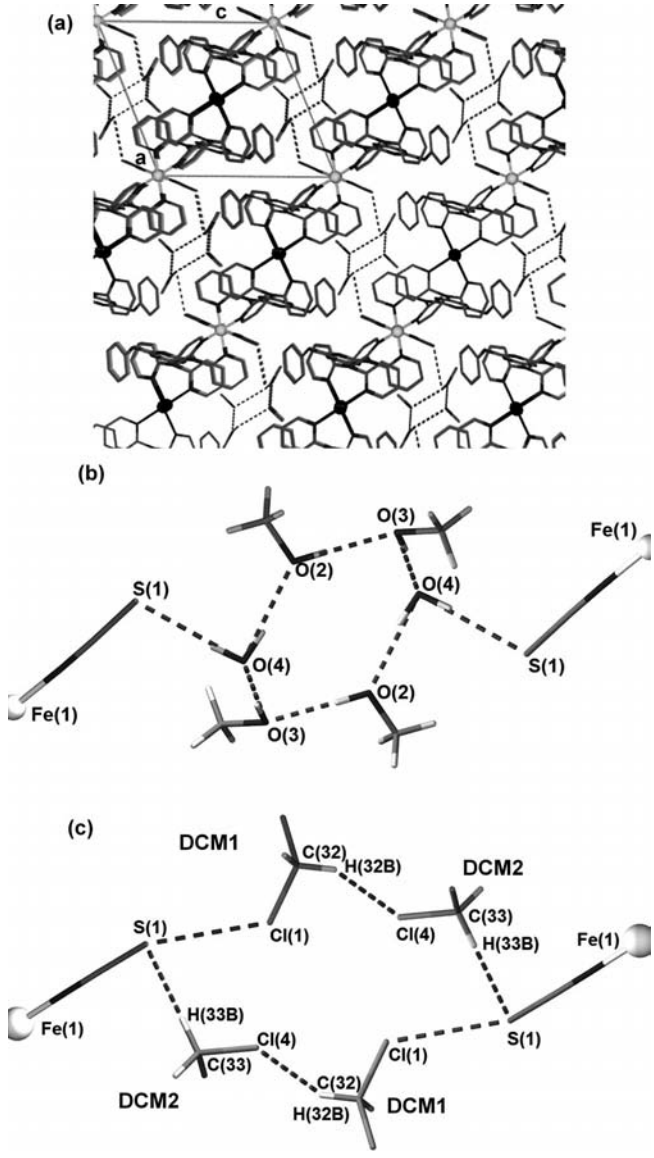


Figure 13. (a) Packing diagram for **5a**, showing a view along the *b*-axis, with the localised $(H_2O)_2(CH_3OH)_4$ hydrogen-bonding network (hydrogen atoms have been omitted for clarity); (b) localised $(H_2O)_2(CH_3OH)_4$ hydrogen-bonding network in **5**; (c) analogous solvent pocket in **6** incorporating lattice dichloromethane molecules, as described in the text (here, dashed lines represent closest contacts, not hydrogen bonds). Fe1 atoms are shown as white spheres, and Fe2 atoms are shown as black spheres.

Turning now to $NCSe^-$ effects in **7** and **8**, within their extended structures, close Se···Se contacts are noted between Fe1 centres on adjacent chains (see Table 5), and also

  

between Fe2 centres on adjacent chains, such that Se1···Se1 and Se2···Se2 interactions form an extended intermolecular network between 1D chains. Other interchain contacts include a face-to-face π-stacking interaction occurring between Ω5 moieties of diagonally adjacent 1D chains (see Table S7). Se···O interactions are noted between both $NCSe1^-$ ligands and $O_{quinol}$ on adjacent chains; in **7a** the length of this contact is 3.329(6) Å and for **8a** it is 3.34(1) Å (Table S7).

Finally, we note that interchain S···S and Se···Se interactions of the kind just discussed likewise occur in the DPPyT-bridged complexes **1**, **2** and **4**, respectively, with contact distances given in the Results section above. Furthermore, in relation to the $NCX^-$ groups, and as found for the other 1D compounds described here, X···$centroid_{triazine}$ distances (Tables 1, 2 and 3) are indicative of S···π interactions between the electron-rich S or Se atoms of the $NCX^-$ ligands and the electron-deficient *s*-triazine ring of the DPPyT ligand.[26] Such interactions were also noted in the related monomeric compound *trans*-[$Fe^{II}$(dpyatriz)$_2$(NCS)$_2$][26] [where dpyatriz = $N^2$,$N^2$,$N^4$,$N^4$,$N^6$,$N^6$-hexa(pyridin-2-yl)-1,3,5-triazine-2,4,6-triamine] and the 1D chain series *trans*-[$Fe^{II}$(cddt)(NCX)$_2$]·Solvent.[13] Although the ligand DPPyT was designed to include a number of aromatic moieties in order to promote intermolecular interactions of the π–π type between 1D chains, such interactions do not occur extensively here. An edge-to-face C–H···π interaction is noted between the Ω3 and Ω4 pyridyl rings on diagonally adjacent chains, and here the closest C···C contact in **1a** is 3.69(1) Å, in **2a** is 3.799(6) Å and in **4a** is 3.782(6) Å.

### *(iii) Solvent Effects*

In the DPPyT derivatives, solvent molecules are located in similar positions in the lattice for **1**, **2** and **4**, and X···O interactions are present between $NCX1^-$ ligands and lattice methanol molecules for **2** and **4** (see Table S1), in a related manner to that discussed in *(ii)* for **5**. The effects, upon the magnetic and photomagnetic data, of partial or full desolvation of the $2.5CH_2Cl_2$ molecules in **1** {*trans*-[$Fe^{II}$(NCS)$_2$(DPPyT)]·$2.5CH_2Cl_2$}, viz. $\mathbf{1}_{\alpha}$, $\mathbf{1}_{\beta}$ and $\mathbf{1}_{\gamma}$, have been described earlier. Unfortunately, in comparison to recent work on dinuclear $Fe^{II}$ SCO complexes that employed related ligands to those used here,[36] where we were able to structurally characterise some of the partial $CH_2Cl_2$ solvates, we do not have crystal structure data here on any of the desolvated forms due to loss of crystallinity. The solvent-dependent observations on **1** therefore remain descriptive. In the complex **5** {*trans*-[$Fe^{II}$(NCS)$_2$(DPT)]·$2CH_3OH$·$H_2O$} the $T_{1/2}$ value moved 25 K to a lower temperature upon full desolvation ($\mathbf{5}_{\alpha}$) whereas the spin transition remained "half". Thus, it is reasonable to conclude that the Fe1 and Fe2 sites retain their parental symmetry and the –LS–HS–LS–HS– states remain ordered below $T_{1/2}$ in the fully desolvated form, the change in $T_{1/2}$ being largely due to the loss of the interchain H-bonded solvent network present in **5**. In contrast, the partially desolvated form $\mathbf{5}_{\beta}$, coated in grease and used in LIESST studies, showed a more gradual, half-spin transition, probably due to disruption of the connecting MeOH·$H_2O$ network.

## Conclusions

We have described the synthesis and characterisation of three new *s*-triazinebis(dpa) ligands, DPPyT, DPT and DQT, containing different substituents on the *s*-triazine ring, and several SCO $Fe^{II}$ coordination complexes of type *trans*-[$Fe^{II}$(NCX)$_2$(L)$_n$] incorporating L as a bridging ($n$ = 1) or terminal ($n$ = 2) chelator, in 1D and 0D complexes, respectively. It is noted that generally solvation and dimensionality of the obtained products is unpredictable and governed by subtle factors. The ligand DPPyT has afforded a less diverse range of products in comparison to DPT and DQT, giving only linear 1D chains in spite of solvent or $NCX^-$ ligands used in *trans*-[$Fe^{II}$(NCX)$_2$(DPPyT)]·Solvent systems, whereas the (perhaps) more flexible ligands DPT and DQT have given a range of linear and zig-zag 1D chains, as well as two monomeric compounds.

Compounds **5** and **6** show a "half" SCO in magnetic susceptibility studies, whereas X-ray crystal structures, solved at low temperatures, reveal ordered HS and LS $Fe^{II}$ centres that alternate along linear 1D chains. In contrast, the 1D complexes **1**, **2**, **3**, **4**, **7** and **8**, the latter two displaying zig-zag chains, and the monomers **9** and **10**, show full HS-to-LS spin transitions. Magnetic susceptibility and LIESST susceptibility measurements, in conjunction with VTPXRD studies (on **2** and **6**) have found that all the 1D materials undergo continuous and gradual spin transitions, and it is suggested that low cooperativity is inherent in these types of materials. LIESST measurements taken on the parent solvate **1**, and samples of **1** desolvated under different regimes, revealed marked differences in magnetic character. The metastable, light-induced HS state is more stable for a sample of **1** that contains less lattice dichloromethane ($\mathbf{1}_{\beta}$), as determined by LIESST experiments. LIESST measurements on **6** and a partially desolvated sample of **5** (viz. $\mathbf{5}_{\beta}$) give characteristic $T$(LIESST) temperatures of 52 K and 58 K, respectively, and $\mathbf{5}_{\beta}$ shows a greater photoconversion efficiency at low temperatures than **6**. These compare to the $T$(LIESST) for $\mathbf{1}_{\beta}$ of 30 K.

Finally, whereas the present work is descriptive and phenomenological, a few brief comments are warranted on how SCO compounds of the present type fit in, or relate to, the recent quantitative ab initio calculations of Robert et al.[8,9] that point to cooperativity/hysteresis in bistable, crystalline SCO $Fe^{II}$ monomers essentially arising from the Madelung fields produced by the electrostatic effect, upon the $Fe^{II}$ molecules, of the surrounding crystal environment. The model was capable of deducing the cooperativity factors calculated for hysteresis loops by Slichter and Drickamer who used regular solution theory.[37] It also complements the Spiering model for elastic driven (intermolecular energy) cooperativity.[38] Much of the emphasis in this paper on using covalent bridges, in coordination polymers,

  

and intermolecularly related communication networks, such as weak van der Waal forces, to enhance cooperativity, has not worked out in practice. Supramolecular interactions of the kind described here, such as aromatic forces, π–π stacking, H-bonding and solvent effects, are known to affect cooperativity, often leading to hysteretic behaviour,[5,39] but that is not the case here. Indeed, many such interactions are regarded by Robert and co-workers as being primarily to stabilise the 3D crystal lattice structure, the latter then providing the electrostatic forces that drive cooperativity.

The monomeric complex **10** shows a $\chi_M T$ vs. $T$ behaviour that is non-hysteretic and similar to that found by Létard et al.[39] for the monomeric complex *cis*-[Fe(pm-aza)-$(NCS)_2$] {where pm-aza = *N*-(2′-pyridylmethylene)-4-(phenylazo)aniline} for which related compounds showed stronger cooperativity and large hysteresis loops. The intermolecular cooperativity factor, $\Gamma$, for *cis*-[Fe(pm-aza)-$(NCS)_2$], deduced by Robert et al. was ca. 0 K, whereas the analogue with $\Delta T$ = 40 K had $\Gamma$ = 444 K. The $\Gamma$ value for **10** will be likewise negligible and remains to be tested by using the structural data provided here.

Coordination polymeric SCO materials of the present 1D kind, **1**–**8**, or of the iconic and highly hysteretic [Fe(4R-1,2,4-triazole)$_3$](anion)$_2$ kind,[6] do not fit into Robert's present calculations, as far as we can judge, and this remains a calculational challenge for the future. As well as Madelung potentials induced on the 1D chains, and on the constituent $Fe^{II}$ chromophores in their LS and HS forms, by the lattice, the effects of covalently bridged nearest neighbours needs to be considered. The ordered –LS–HS–LS–HS– forms observed here, for some of the complexes, present an intriguing challenge for such calculations. Can they be rationalised or even predicted beforehand? Meanwhile, Kepert is using the mean field model[37] to successfully simulate hysteresis loops in a variety of polynuclear SCO materials, including two-step transitions, in which the covalent bridging ligands are simply regarded as springs.[40] From an experimental perspective, high-resolution crystallography and photocrystallography would be useful on polynuclear $Fe^{II}$ crossover systems of the present 1D type to obtain electron densities of the kind recently observed for monomers,[41,42] and thus identify intermolecular interactions and provide back-up information for calculations of cooperativity.

## Experimental Section

**General:** All reagents and solvents were purchased from Sigma–Aldrich Pty. Ltd. and used as received. The starting material cddt was synthesised based on a previously published method.[23] $^1$H and $^{13}$C NMR spectra were recorded with a Bruker DPX 300 300 MHz NMR spectrometer. IR spectra were recorded with a Bruker Equinox 55 FT-IR fitted with a Judson MCT detector and Specac "Golden Gate" diamond ATR. Low-resolution mass spectra were recorded with a Micromass (now Waters) Platform II QMS connected to a Waters Alliance 2690 LC system for automatic flow injections, whereas high-resolution mass spectra were recorded with an Agilent 6220 Accurate Mass LC-TOF system with Agilent 1200 Series LC by using a purine/HP0921 mix as the reference compound. Melting points were determined with a Bibby Stuart Scientific melting point apparatus SMP3. Microanalyses were performed by Campbell Microanalytical Laboratory, Department of Chemistry, University of Otago, Dunedin, New Zealand.

**Magnetic Susceptibility and Photomagnetic Measurements:** Magnetic susceptibility data were collected with a Quantum Design MPMS 5 SQUID magnetometer under an applied field of 1 T. The solvated crystalline samples were placed in a quartz tube and great care was taken to avoid any solvent loss. Desolvated samples of **1** and **5** were placed in gel capsules held within plastic straws. Care was taken to allow long thermal equilibration times at each temperature point, and warming and cooling modes were employed to detect HS thermal trapping.

Photomagnetic characterisation for samples of **1** and **5** was carried out at CNRS, Université de Bordeaux, ICMCB, with a Spectrum Physics Series 2025 Kr+ laser coupled through an optical fibre into the cavity of the MPMS-55 Quantum design SQUID magnetometer operating at 2 T. Samples were prepared as a thin layer (ca. 0.1 mg) to promote full penetration of the irradiated light. The sample weight was obtained by comparing its thermal spin transition behaviour with a heavier and accurately weighed sample.[12] The sample was first slowly cooled to 10 K by ensuring that potential trapping of HS species at low temperatures did not occur. Irradiation to photosaturation was carried out a number of times at different wavelengths (i.e. 337/356.4, 406.7/415.4, 532, 647.1/676.4, 752.5/799.3 nm) to determine which source was most efficient at a power intensity of 5 mW cm$^{-2}$ (to prevent warming of the sample). Samples were then cooled to 10 K and irradiated with green light ($\lambda$ = 532 nm at 5 mW cm$^{-2}$ was found to be the most efficient) until photosaturation was reached. Then, in the absence of irradiation, the temperature was increased at a rate of 0.3 K min$^{-1}$. The extreme of the $\delta\chi_M T/\delta T$ vs. $T$ plot gave the $T$(LIESST) values for $\mathbf{1}_\beta$ and $\mathbf{5}_\beta$, defined as the temperature for which the light-induced HS information is erased.[12] At 10 K, the samples $\mathbf{1}_\beta$ and $\mathbf{5}_\beta$ were again irradiated to photosaturation, and in the absence of irradiation the relaxation kinetics at 10, 25, 32, 35, 38 and 40 K were measured for $\mathbf{1}_\beta$; for sample $\mathbf{1}_\gamma$ relaxation kinetics were measured in this manner only at 10 K. The relaxation kinetics were measured at 10, 20, 45, 50, 54, 56, 60, 65, 70 and 75 K for $\mathbf{5}_\beta$. See Supporting Information for further details.

**Mössbauer Effect Measurements:** These were carried out by using a conventional constant acceleration drive with a symmetric sawtooth waveform at 77 and 295 K in the School of Physics, Monash University. Fitting of spectra used both Voigtian and Lorentzian lineshape functions from the Recoil analysis software (Intelligent Scientific Applications, Inc.). The instrument was calibrated with α-iron. Isomer shifts are referenced to α-iron at room temperature.

**Crystallographic Data Collection and Refinement:** Crystallographic data and parameters for **1a**–**c**, **2a**–**c** and **4a**–**c** are summarised in Tables 7, 8 and 9. Single-crystal diffraction data for these structures were collected with a Bruker APEX X8 diffractometer by using Mo-$K_\alpha$ ($\lambda$ = 0.71073 Å) radiation and equipped with an Oxford Instruments nitrogen gas cryostream. Crystals were mounted on glass fibres in a small amount of oil. For **1a**, a single crystal was quench-cooled to 250(2) K, with subsequent slow cooling to 160(2) K for **1b** and 100(2) K for **1c**. For **2a**, a single crystal was quench-cooled to 123(2) K, and subsequently a single crystal was cooled to 200(2) K for **2b** and then slowly heated to 250(2) K for **2c**. For **4a**, a single crystal was quench-cooled to 100(2) K, and subsequently a single crystal was quench-cooled to 240(2) K for **4b**,

  

followed by slow heating to 260(2) K for **4c**. Initial diffraction-data analysis was performed by using the APEX2 software package.[43] The structures were solved by using SHELXS and refined by using SHELXL-97 within the graphical interface X-Seed.[44] All non-hydrogen atoms in the structures were refined anisotropically (unless specified), and hydrogen atoms were generated by using the riding model. Special refinement details are located in the Supporting Information. Data for **2d**, **2e**, **2f**, **2g** and **5**, **6**, **7**, **8** and **10** were collected at the Australian Synchrotron by using the MX1 beamline (Tables 10, 11 and 12). For **2d**–**g** the beamline was operating at $\lambda$ = 0.77487 Å, and for **5**, **6**, **7**, **8** and **10** the beamline was operating at $\lambda$ = 0.77506 Å. The collection temperature was maintained at specified temperatures by using an open-flow $N_2$ cryostream. A sample of **2** was mounted at 260 K whereupon data for **2d** was collected, and was then cooled slowly from this temperature, at each collection point allowing long thermal equilibration times. Samples **5** and **6** were quench-cooled to 100(2) K and then warmed to higher temperatures. Sample of **7**, **8** and **10** were quench-cooled

Table 7. Crystallographic data for **1**.

| | **1a** | **1b** | **1c** |
|---|---|---|---|
| Empirical formula | $C_{32.50}H_{25}Cl_5FeN_{12}OS_2$ | $C_{32.50}H_{25}Cl_5FeN_{12}OS_2$ | $C_{32.50}H_{25}Cl_5FeN_{12}OS_2$ |
| Formula mass /g mo$l^{-1}$ | 896.86 | 896.86 | 896.86 |
| $T$ /K | 100 | 160 | 250 |
| Crystal system | monoclinic | monoclinic | monoclinic |
| Space group | $P2_1/c$ | $P2_1/c$ | $P2_1/c$ |
| Z | 4 | 4 | 4 |
| $a$ /Å | 17.3826(9) | 17.4517(7) | 17.6580(5) |
| $b$ /Å | 14.3349(7) | 14.2927(5) | 14.2275(5) |
| $c$ /Å | 15.4710(8) | 15.6593(6) | 16.3555(5) |
| $\beta$ /° | 97.310(2) | 97.822(2) | 99.313(2) |
| $V$ /Å$^3$ | 3823.7(3) | 3869.6(3) | 4054.8(2) |
| $\rho_{calcd.}$ /g cm$^{-3}$ | 1.558 | 1.539 | 1.469 |
| $\mu$ /mm$^{-1}$ | 0.900 | 0.889 | 0.848 |
| Collected data | 21945 | 20447 | 28162 |
| Unique data | 6641 | 6694 | 7116 |
| Observed data | 4144 | 3960 | 3668 |
| Restraints | 83 | 39 | 7 |
| Parameters | 563 | 553 | 457 |
| $R$(int) | 0.0720 | 0.0681 | 0.0736 |
| $R(F)$ /% | 0.0813, | 0.0772, | 0.1131, |
| [$I > 2\sigma(I)$, all][a] | 0.1334 | 0.1352 | 0.1896 |
| $wR^2(F^2)$ /% | 0.2250, | 0.2162, | 0.3347, |
| [$I > 2\ \sigma\ (I)$, all][b] | 0.2645 | 0.2578 | 0.3914 |
| GoF | 1.035 | 1.058 | 1.304 |

[a] $R = \Sigma||F_o| - |F_c||/\Sigma|F_o|$. [b] $wR^2 = [\Sigma w(F_o^2 - F_c^2)^2/\Sigma(F_o^2)^2]^{1/2}$.

Table 8. Crystallographic data for **2**.

| | **2a** | **2b** | **2c** |
|---|---|---|---|
| Empirical formula | $C_{32.50}H_{24}Cl_6FeN_{12}O_{1.50}S_2$ | $C_{32.50}H_{24}Cl_6FeN_{12}O_{1.50}S_2$ | $C_{32.50}H_{24}Cl_6FeN_{12}O_{1.50}S_2$ |
| Formula mass /g mo$l^{-1}$ | 939.31 | 939.31 | 939.31 |
| $T$ /K | 123 | 200 | 250 |
| Crystal system | monoclinic | monoclinic | monoclinic |
| Space group | $P2_1/c$ | $P2_1/c$ | $P2_1/c$ |
| Z | 4 | 4 | 4 |
| $a$ /Å | 17.3588(8) | 17.3885(14) | 17.5612(12) |
| $b$ /Å | 14.2979(6) | 14.3236(8) | 14.3279(9) |
| $c$ /Å | 15.7634(6) | 16.0358(13) | 16.3272(14) |
| $\beta$ /° | 97.812(2) | 97.959(2) | 98.768(3) |
| $V$ /Å$^3$ | 3876.1(3) | 3955.5(5) | 4060.2(5) |
| $\rho_{calcd.}$ /g cm$^{-3}$ | 1.610 | 1.577 | 1.537 |
| $\mu$ /mm$^{-1}$ | 0.959 | 0.940 | 0.916 |
| Collected data | 27121 | 11455 | 21297 |
| Unique data | 6819 | 6478 | 7142 |
| Observed data | 5247 | 3112 | 3040 |
| Restraints | 10 | 37 | 39 |
| Parameters | 547 | 547 | 527 |
| $R$(int) | 0.0428 | 0.0705 | 0.1086 |
| $R(F)$ /% | 0.0490, | 0.0782, | 0.0929, |
| [$I > 2\sigma(I)$, all][a] | 0.0681 | 0.1714 | 0.2054 |
| $wR^2(F^2)$ /% | 0.1244, | 0.1893, | 0.2644, |
| [$I > 2\ \sigma\ (I)$, all][b] | 0.1374 | 0.2391 | 0.3396 |
| GoF | 1.035 | 1.010 | 1.017 |

[a] $R = \Sigma||F_o| - |F_c||/\Sigma|F_o|$. [b] $wR^2 = [\Sigma w(F_o^2 - F_c^2)^2/\Sigma(F_o^2)^2]^{1/2}$.

  

to 250(2) K, and then slowly cooled for subsequent collections. Data were collected by using the Blue Ice software.[45] Initial data processing was carried out by using the XDS package.[46] All structures were solved by direct methods using SHELXS-97.[44] Least-squares refinements against $F^2$ were carried out by using SHELXL--97; the program X-Seed was used as a graphical interface.[44] All hydrogen atoms were placed in idealised positions and refined by using a riding model except for **5** where hydrogen atoms on the water molecule were located in the difference map. Asymmetric unit figures for all structures are located in the Supporting

Table 9. Crystallographic data for **4**.

| | **4a** | **4b** | **4c** |
|---|---|---|---|
| Empirical formula | $C_{32.50}H_{24}Cl_6FeN_{12}O_{1.50}Se_2$ | $C_{32.50}H_{24}Cl_6FeN_{12}O_{1.50}Se_2$ | $C_{32.50}H_{24}Cl_6FeN_{12}O_{1.50}Se_2$ |
| Formula mass /g mo$l^{-1}$ | 1033.11 | 1033.11 | 1033.11 |
| $T$ /K | 100 | 240 | 260 |
| Crystal system | monoclinic | monoclinic | monoclinic |
| Space group | $P2_1/c$ | $P2_1/c$ | $P2_1/c$ |
| Z | 4 | 4 | 4 |
| $a$ /Å | 17.4057(3) | 17.472(2) | 17.5054(4) |
| $b$ /Å | 14.2760(2) | 14.344(2) | 14.3346(4) |
| $c$ /Å | 15.9363(3) | 16.263(2) | 16.4222(4) |
| $\beta$ /° | 98.438(10) | 98.358(6) | 98.640(10) |
| $V$ /Å$^3$ | 3917.05(11) | 4032.9(9) | 4074.11(18) |
| $\rho_{calcd.}$ /g cm$^{-3}$ | 1.752 | 1.702 | 1.684 |
| $\mu$ /mm$^{-1}$ | 2.701 | 2.623 | 2.597 |
| Collected data | 26864 | 38263 | 37092 |
| Unique data | 8950 | 9241 | 8992 |
| Observed data | 6231 | 5432 | 5053 |
| Restraints | 7 | 7 | 22 |
| Parameters | 535 | 535 | 530 |
| $R$(int) | 0.0498 | 0.0583 | 0.0516 |
| $R(F)$ /% | 0.0499, | 0.0560, | 0.0636, |
| [$I>2\sigma(I)$, all][a] | 0.0845 | 0.1141 | 0.1287 |
| $wR^2(F^2)$ /% | 0.1142, | 0.1393, | 0.1664, |
| [$I>2\ \sigma\ (I)$, all][b] | 0.1292 | 0.1649 | 0.2004 |
| GoF | 1.010 | 1.029 | 1.038 |

[a] $R = \Sigma||F_o| - |F_c||/\Sigma|F_o|$. [b] $wR^2 = [\Sigma w(F_o^2 - F_c^2)^2/\Sigma(F_o^2)^2]^{1/2}$.

Table 10. Crystallographic data for **5**, **6**.

| | **5a** | **5b** | **6a** | **6b** |
|---|---|---|---|---|
| Empirical formula | $C_{33}H_{31}FeN_{11}O_4S_2$ | $C_{33}H_{31}FeN_{11}O_4S_2$ | $C_{33}H_{25}Cl_4FeN_{11}O_2S_2$ | $C_{33}H_{25}Cl_4FeN_{11}O_2S_2$ |
| Formula mass /g mo$l^{-1}$ | 765.66 | 765.66 | 869.42 | 869.42 |
| $T$ /K | 100 | 190 | 100 | 250 |
| Crystal system | triclinic | triclinic | triclinic | triclinic |
| Space group | $P\bar{1}$ | $P\bar{1}$ | $P\bar{1}$ | $P\bar{1}$ |
| Z | 2 | 2 | 2 | 2 |
| $a$ /Å | 12.041(4) | 12.156(5) | 12.196(2) | 12.33(3) |
| $b$ /Å | 12.681(2) | 12.718(4) | 12.817(1) | 12.910(7) |
| $c$ /Å | 12.810(2) | 12.894(3) | 13.092(2) | 13.168(9) |
| $\alpha$ /° | 85.303(4) | 84.555(5) | 84.43(1) | 84.00(4) |
| $\beta$ /° | 67.567(9) | 68.771(11) | 65.791(6) | 66.44(5) |
| $\gamma$ /° | 87.748(7) | 87.536(6) | 86.60(1) | 86.90(5) |
| $V$ /Å$^3$ | 1801.8(7) | 1849.7(10) | 1857.3(5) | 1911(5) |
| $\rho_{calcd.}$ /g cm$^{-3}$ | 1.411 | 1.375 | 1.555 | 1.511 |
| $\mu$ /mm$^{-1}$ | 0.588 | 0.573 | 0.855 | 0.831 |
| Collected data | 19910 | 20432 | 20789 | 21195 |
| Unique data | 5140 | 5269 | 5324 | 5461 |
| Observed data | 4746 | 4691 | 4612 | 4371 |
| Restraints | 2 | 2 | 0 | 0 |
| Parameters | 474 | 473 | 483 | 483 |
| $R$(int) | 0.0448 | 0.0294 | 0.0689 | 0.0459 |
| $R(F)$ /% | 0.0513, | 0.0560, | 0.0608, | 0.0678, |
| [$I>2\sigma(I)$, all][a] | 0.0545 | 0.0617 | 0.0688 | 0.0835 |
| $wR_2(F^2)$ /% | 0.1339, | 0.1459, | 0.1687, | 0.1853, |
| [$I>2\sigma\ (I)$, all][b] | 0.1364 | 0.1501 | 0.1747 | 0.1982 |
| GoF | 1.029 | 1.027 | 1.022 | 1.039 |

[a] $R = \Sigma||F_o| - |F_c||/\Sigma|F_o|$. [b] $wR^2 = [\Sigma w(F_o^2 - F_c^2)^2/\Sigma(F_o^2)^2]^{1/2}$.

  

Table 11. Crystallographic data for **7**, **8**.

| | **7a** | **7b** | **8a** | **8b** |
|---|---|---|---|---|
| Empirical formula | $C_{32.5}H_{24}Cl_2FeN_{11}O_2Se_2$ | $C_{32.5}H_{24}Cl_2FeN_{11}O_2Se_2$ | $C_{32.5}H_{25}Cl_2FeN_{11}O_{2.5}Se_2$ | $C_{32.5}H_{25}Cl_2FeN_{11}O_{2.5}Se_2$ |
| Formula mass /g mol$^{-1}$ | 885.30 | 885.30 | 894.30 | 894.30 |
| $T$ /K | 100 | 250 | 100 | 250 |
| Crystal system | monoclinic | monoclinic | monoclinic | monclinic |
| Space group | $C2/c$ | $C2/c$ | $C2/c$ | $C2/c$ |
| Z | 8 | 8 | 8 | 8 |
| $a$ /Å | 12.842(2) | 12.994(3) | 12.820(1) | 13.024(8) |
| $b$ /Å | 21.663(10) | 21.772(4) | 21.621(7) | 21.879(6) |
| $c$ /Å | 27.453(6) | 27.952(2) | 27.357(3) | 27.93(2) |
| $\alpha$ /° | 90 | 90 | 90 | 90 |
| $\beta$ /° | 96.328(3) | 96.06(2) | 96.36(3) | 96.12(3) |
| $\gamma$ /° | 90 | 90 | 90 | 90 |
| $V$ /Å$^3$ | 7591(4) | 7864(2) | 7536(3) | 7881(8) |
| $\rho_{calcd.}$ /g cm$^{-3}$ | 1.549 | 1.496 | 1.576 | 1.507 |
| $\mu$ /mm$^{-1}$ | 2.501 | 2.415 | 2.521 | 2.411 |
| Collected data | 42569 | 44337 | 42805 | 43828 |
| Unique data | 5918 | 6125 | 5827 | 6049 |
| Observed data | 4660 | 4527 | 4677 | 4401 |
| Restraints | 41 | 47 | 96 | 17 |
| Parameters | 489 | 489 | 500 | 475 |
| $R$(int) | 0.0848 | 0.0728 | 0.1329 | 0.1072 |
| $R(F)$ /% | 0.0814, | 0.0792, | 0.0767, | 0.0744, |
| $[I > 2\sigma(I)$, all][a] | 0.1015 | 0.1052 | 0.0937 | 0.1038 |
| $wR_2(F^2)$ /% | 0.2172, | 0.2127, | 0.2024, | 0.1940, |
| $[I > 2\sigma\ (I)$, all][b] | 0.2333 | 0.2326 | 0.2166 | 0.2161 |
| GoF | 1.036 | 1.046 | 1.030 | 1.041 |

[a] $R = \Sigma||F_o| - |F_c||/\Sigma|F_o|$. [b] $wR^2 = [\Sigma w(F_o^2 - F_c^2)^2/\Sigma(F_o^2)^2]^{1/2}$.

Table 12. Crystallographic data for **10**.

| | **10a** | **10b** | **10c** |
|---|---|---|---|
| Empirical formula | $C_{30.8}H_{24.2}Fe_{0.5}N_{10}O_{1.8}Se$ | $C_{30.5}H_{23}Fe_{0.5}N_{10}O_{1.5}Se$ | $C_{30.5}H_{23}Fe_{0.5}N_{10}O_{1.5}Se$ |
| Formula mass /g mol$^{-1}$ | 670.09 | 660.47 | 660.47 |
| $T$ /K | 100 | 200 | 250 |
| Crystal system | triclinic | triclinic | triclinic |
| Space group | $P\bar{1}$ | $P\bar{1}$ | $P\bar{1}$ |
| Z | 2 | 2 | 2 |
| $a$ /Å | 8.799(5) | 8.859(3) | 8.95(1) |
| $b$ /Å | 12.815(2) | 12.886(2) | 12.942(6) |
| $c$ /Å | 13.166(5) | 13.188(3) | 13.190(8) |
| $\alpha$ /° | 84.233(7) | 84.279(5) | 84.46(2) |
| $\beta$ /° | 77.061(2) | 77.65(2) | 78.40 (4) |
| $\gamma$ /° | 86.762(2) | 86.77(2) | 86.76(6) |
| $V$ /Å$^3$ | 1438.7(10) | 1462.4(6) | 1489(2) |
| $\rho_{calcd.}$ /g cm$^{-3}$ | 1.547 | 1.500 | 1.473 |
| $\mu$ /mm$^{-1}$ | 1.596 | 1.568 | 1.540 |
| Collected data | 15921 | 16185 | 16645 |
| Unique data | 4092 | 4183 | 4268 |
| Observed data | 3622 | 3464 | 3410 |
| Restraints | 3 | 13 | 13 |
| Parameters | 409 | 405 | 405 |
| $R$(int) | 0.0543 | 0.0594 | 0.0595 |
| $R(F)$ /% | 0.0624, | 0.0624, | 0.0671, |
| $[I > 2\sigma(I)$, all][a] | 0.0687 | 0.0740 | 0.0817 |
| $wR_2(F^2)$ /% | 0.1711, | 0.1731, | 0.1861, |
| $[I > 2\sigma\ (I)$, all][b] | 0.1761 | 0.1830 | 0.1994 |
| GoF | 1.051 | 1.045 | 1.038 |

[a] $R = \Sigma||F_o| - |F_c||/\Sigma|F_o|$. [b] $wR^2 = [\Sigma w(F_o^2 - F_c^2)^2/\Sigma(F_o^2)^2]^{1/2}$.

Information. CCDC-788815 to -788838 contain the supplementary crystallographic data for this paper. These data can be obtained free of charge from The Cambridge Crystallographic Data Centre via www.ccdc.cam.ac.uk/data_request/cif.

**Powder Synchrotron X-ray Diffraction:** A microcrystalline sample of **2**, damp with a mixture of chloroform and methanol, was loaded into a soda-glass Mark tube of 0.5 mm diameter and sealed with wax. Diffraction data were collected at the Powder Diffraction

  

Beamline (10-BM-1) at the Australian Synchrotron. The glass capillary was mounted and aligned concentrically to the rotation of the three-axis diffractometer, and data were collected by using a MYTHEN strip detector. The wavelength was determined to be 1.00049 Å by using NIST standard 660a, $LaB_6$. The sample temperature was controlled by using an open-flow $N_2$ cryostream, and data were collected at 180 s exposure times at five degree intervals from 250 K to 100 K. Le Bail analyses of the variable-temperature diffraction data were performed within RIETICA.[29] Details of the refinements are included in the Supporting Information, Table S8. A pulverised sample of *trans*-$[Fe^{II}(NCS)_2(DQT)]\cdot 2CH_2Cl_2$ (**6**) was loaded in a polyimide capillary of 0.8 mm diameter and kept in an inert helium atmosphere for the duration of the experiments.[47] The X-rays ($\lambda$ = 0.61832 Å) available at the 1-BM beamline at the Advanced Photon Source at Argonne National Laboratory were used in combination with an MAR-345 imaging plate (IP) detector to record diffraction patterns. The sample temperature was controlled by using an Oxford Cryosystems Cryostream Plus, and data were collected in 6 s exposures upon a quench-cooled sample with continuous warming from ca. 103 K to ca. 283 K at 100 K $h^{-1}$. This corresponds to the collection of diffraction images at 3 K intervals. The raw images were processed by using Fit-2D.[48,49] The sample-to-detector distance and tilt of the IP relative to the beam were refined by using an $LaB_6$ standard. Le Bail analyses of the variable-temperature diffraction data were performed within GSAS.[50] Details of the refinements are included in Table S9.

## Syntheses

### Organic Ligands

**1-[4,6-Bis(dipyridin-2-ylamino)-1,3,5-triazin-2-yl]pyridin-4(1*H*)-one (DPPyT):** The compounds cddt (1.5 g, 3.3 mmol) and 4-hydroxypyridine (1 g, 10.5 mmol) were dissolved in dimethyl sulfoxide (5 mL). To this, *N*,*N*-diisopropylethylamine (4 mL, 22.9 mmol) was added, and the biphasic mixture was heated to 90 °C with vigorous stirring for 4 h. Distilled water (50 mL) was added to the obtained golden brown solution. The resultant white precipitate was isolated by filtration and washed with THF and ethanol (1.2 g, 70.8%). M.p. 307.2–307.9 °C. IR: $\tilde{\nu}$ = 3058 (w), 996 (m), 803 (w), 774 (w), 1587 (m), 1574 (m), 1472 (m), 1550 (w), 1526 (m), 1091 (m) $cm^{-1}$. ESI-MS: *m*/*z* = 513 [M + H]. $^1$H NMR ([D$_6$]DMSO, 298 K): $\delta$ = 8.37 (ddd, *J* = 4.8, 1.8, 0.9 Hz, 4 H, py), 8.17 (m, 2 H, pyridone), 7.91 (ddd, *J* = 8.1, 7.2, 1.8 Hz, 4 H, py), 7.65 (dt, *J* = 8.1, 0.9 Hz, 4 H, py), 7.29 (ddd, *J* = 7.2, 4.8, 1.2 Hz, 4 H, py), 6.24 (m, 2 H, pyridone) ppm. $^{13}$C NMR ([D$_6$]DMSO, 298 K): $\delta$ = 179.41, 165.62, 161.19, 154.28, 148.32, 137.73, 133.79, 122.77, 121.75, 117.89 ppm. $C_{28}H_{20}N_{10}O$ (512.53): calcd. C 65.62, H 3.93, N 27.33; found C 64.95, H 3.89, N 27.07.

**6-Phenoxy-$N^2$,$N^2$,$N^4$,$N^4$-tetra-2-pyridinyl-1,3,5-triazine-2,4-diamine (DPT):** The compounds cddt (1.75 g, 3.85 mmol) and phenol (3.5 g, 37.2 mmol) were dissolved in dimethyl sulfoxide (6 mL). To this, diisopropylamine (5 mL, 28.7 mmol) was added, and the biphasic mixture was heated to 90 °C with vigorous stirring for 5 h. The resultant dark brown solution was allowed to cool, diluted with distilled water (30 mL), and then extracted with chloroform (3 × 50 mL). The volume of the organic phase was reduced in vacuo to leave a dark brown oil, which was purified by column chromatography ($SiO_2$; tetrahydrofuran/dichloromethane, 1:1; $R_f$ = 0.65) to yield an off-white powder. The white powder was isolated by filtration and then dissolved in a minimum of hot acetone (5 mL); distilled water (80 mL) was added until a white precipitate began to form. After 3 h, a white solid was isolated by filtration and washed with distilled water (1.39 g, 70.4%). M.p. 223.6–224.1 °C. IR: $\tilde{\nu}$ = 3064 (w), 1587 (m), 1549 (w), 1528 (w), 1490 (s), 1088 (w), 995 (m), 915 (w), 776 (m), 763 (w) $cm^{-1}$. ESI-MS: *m*/*z* = 512 [M + H]. HR-MS: calcd. for $C_{29}H_{22}N_9O$ [M + H] 512.1947; found 512.1941. $^1$H NMR ([D$_6$]DMSO, 298 K): $\delta$ = 8.25 (ddd, *J* = 4.8, 1.8, 0.9 Hz, 4 H, py), 7.75 (ddd, *J* = 8.1, 7.2, 1.8 Hz, 4 H, py), 7.50 (dt, *J* = 8.1, 0.9 Hz, 4 H, py), 7.31 (m, 2 H, phenolic), 7.15 (ddd, *J* = 7.2, 4.8, 0.9 Hz, 4 H, py), 7.13 (m, 3 H, phenolic) ppm. $^{13}$C NMR ([D$_6$]DMSO, 298 K): $\delta$ = 170.00, 166.55, 154.46, 151.60, 148.05, 137.41, 129.01, 125.10, 122.79, 121.52, 121.25 ppm. $C_{29}H_{21}N_9O$ (511.54): calcd. C 68.09, H 4.14, N 24.64; found C 67.62, H 4.52, N 24.38.

**4-[4,6-Bis(dipyridin-2-ylamino)-1,3,5-triazin-2-yloxy]phenol (DQT):** The compounds cddt and (1.54 g, 3.39 mmol) and hydroquinone (3.5 g, 31.7 mmol) were dissolved in dimethyl sulfoxide (5 mL). To this, diisopropylamine (5 mL, 28.7 mmol) was added, and the biphasic mixture was heated to 90 °C with vigorous stirring for 4 h. The resultant dark brown solution was diluted with distilled water (30 mL) and extracted with chloroform (3 × 50 mL). The volume of the organic phase was reduced in vacuo to yield a dark brown oil, which was purified by column chromatography ($SiO_2$; tetrahydrofuran/dichloromethane, 1:1; $R_f$ = 0.68) to yield a beige powder. The beige powder was dissolved in a minimum of hot tetrahydrofuran (5 mL), and hexane (30 mL) was added until an off-white powder precipitated from the solution, which was collected by filtration (0.47 g, 26.3%). M.p. 240.1–240.7 °C. IR: $\tilde{\nu}$ = 2907 (w), 2656 (w), 2324 (w), 2163 (s), 1981 (w), 1577 (m), 1556 (s), 1506 (s), 1460 (s), 1364 (s), 1293 (m), 1199 (m), 1096 (w), 998 (w), 886 (w), 804 (m), 723 (w) $cm^{-1}$. ESI-MS: *m*/*z* = 528 [M + H]. HR-MS: calcd. for $C_{29}H_{22}N_9O_2$ 528.1896; found *m*/*z* = 528.1894. $^1$H NMR ([D$_6$]DMSO, 298 K): $\delta$ = 9.28 (s, 1 H, OH), 8.25 (ddd, *J* = 4.8, 2.1, 0.9 Hz, 4 H, py), 7.74 (ddd, *J* = 8.1, 7.2, 1.8 Hz, 4 H, py), 7.50 (dt, *J* = 8.1, 0.9 Hz, 4 H, py), 7.16 (ddd, *J* = 7.2, 4.8, 1.2 Hz, 4 H, py), 6.92 (m, 2 H, quinol), 6.65 (m, 2 H, quinol) ppm. $^{13}$C NMR ([D$_6$]-DMSO, 298 K): $\delta$ = 170.38, 166.55, 154.50, 154.48, 148.03, 143.87, 137.38, 122.77, 122.18, 121.22, 115.13 ppm.

### $Fe^{II}$ Complexes

#### Polymeric Complexes

***trans*-$[Fe^{II}(NCS)_2(DPPyT)]\cdot 2.5CH_2Cl_2$ (1):** In dichloromethane (3 mL), DPPyT (20 mg, 0.039 mmol) was dissolved. Separately, $Fe(ClO_4)_2$ (10 mg, 0.039 mmol) was dissolved in methanol (3 mL), along with NaNCS (6.3 mg, 0.078 mmol) and a small amount of ascorbic acid to prevent oxidation to $Fe^{III}$. A mixture of methanol/dichloromethane (1:1) (8 mL) was layered carefully on top of the DPPyT solution, and then the methanolic $Fe(NCS)_2$ solution was carefully layered on top of this. The reaction vial was stoppered and the reactants were allowed to slowly diffuse together; over the course of 1 week dark orange block-shaped crystals formed (27.9 mg, 79.9%). IR: $\tilde{\nu}$ = 3419 (br.), 3064 (w), 2058 (s), 1643 (m), 1589 (s), 1541 (s), 1466 (m), 1371 (s), 1241 (m), 1186 (m), 1106 (m), 961 (w), 732 (w) $cm^{-1}$. $C_{30}H_{20}FeN_{12}OS_2\cdot C_{2.5}H_5Cl_5$ (896.87): calcd. C 43.52, H 2.81, N 18.74; found C 43.97, H 2.80, N 19.27.

***trans*-$[Fe^{II}(NCS)_2(DPPyT)]\cdot 2CHCl_3\cdot 0.5CH_3OH$ (2):** The method for **1** was applied by using chloroform in place of dichloromethane. A mixture of methanol/chloroform (1:1) (8 mL) was layered carefully on top of the DPPyT solution, and then the methanolic $Fe(NCS)_2$ solution was carefully layered on top of this. Again, orange block-shaped crystals formed (27.7 mg, yield 75.9%). IR: $\tilde{\nu}$ = 3410 (w), 2057 (s), 1643 (w), 1590 (m), 1541 (m), 1369 (s), 1241 (m), 1148 (m), 959 (w) $cm^{-1}$. $C_{30}H_{20}FeN_{12}OS_2\cdot C_{2.5}H_4Cl_6O_{0.5}$ (939.31): calcd. C 41.56, H 2.58, N 17.89, found C 41.77, H 2.37, N 18.11.

***trans*-$[Fe^{II}(NCSe)_2(DPPyT)]\cdot CH_2Cl_2$ (3):** In methanol (3 mL), $Fe(ClO_4)_2$ (10 mg, 0.039 mmol) was dissolved along with KNCSe

  

(11.2 mg, 0.078 mmol), and the mixture was stirred for 5 min and then allowed to stand at 0 °C for 3 h to precipitate $KClO_4$. After this time, DPPyT (20 mg, 0.039 mmol) was dissolved in dichloromethane (3 mL), and a mixture of methanol/dichloromethane (1:1) (8 mL) was layered carefully on top of the DPPyT solution. The methanolic solution of $Fe(NCSe)_2$ was then layered on top of this, and the reaction vial was stoppered. The reactants were allowed to slowly diffuse together, and over the course of 1 week pale orange block-shaped crystals formed (21.7 mg, 64.4%). IR: $\tilde{\nu}$ = 3343 (w), 2068 (s), 1641 (w), 1590 (m), 1539 (m), 1466 (w), 1366 (s), 1338 (m), 1309 (m), 1187 (m), 1148 (m), 1016 (m), 851 (w), 774 (w) $cm^{-1}$. $C_{30}H_{20}FeN_{12}OSe_2{\cdot}CH_2Cl_2$ (863.26): calcd. C 43.13, H 2.57, N 19.47, found C 43.60, H 2.56, N 20.04.

***trans*-[$Fe^{II}(NCSe)_2$(DPPyT)]·2$CHCl_3$·0.5$CH_3OH$ (4):** The method for **3** was applied by using chloroform in place of dichloromethane. A mixture of methanol/chloroform (1:1) (8 mL) was layered carefully on top of the DPPyT solution. The methanolic solution of $Fe(NCSe)_2$ was layered on top of this, and the reaction vial was stoppered. Again, over the course of 1 week orange block-shaped crystals formed (23.5 mg, 58.4%). IR: $\tilde{\nu}$ = 3316 (w), 2166 (s), 1656 (m), 1565 (s), 1467 (s), 1265 (m), 1142 (m), 1009 (m), 738 (w) $cm^{-1}$. $C_{30}H_{20}FeN_{12}OSe_2{\cdot}C_{2.5}H_4Cl_6O_{0.5}$ (1033.1): calcd. C 37.78, H 2.34, N 16.27, found C 37.50, H 2.27, N 16.05.

***trans*-[$Fe^{II}(NCS)_2$(DPT)]·2$CH_3OH$·$H_2O$ (5):** DPT was dissolved (100 mg, 0.195 mmol) in dichloromethane (2 mL). Separately, $Fe(ClO_4)_2$ (49 mg, 0.195 mmol), NaNCS (32 mg, 0.39 mmol) and ascorbic acid (trace) were dissolved in methanol (3 mL). A mixture of methanol/dichloromethane/water (6:2:1) (8 mL) was layered carefully on top of the DPT solution, and then the methanolic $Fe(NCS)_2$ solution was carefully layered on top of this. The reaction vial was stoppered, and the reactants were allowed to slowly diffuse together. Over the course of 1 week yellow block crystals formed. These were collected and washed with methanol/water (4:1) (134 mg, 89.5%). IR: $\tilde{\nu}$ = 3358 (br.), 2837 (w), 2063 (s), 1583 (m), 1465 (m), 1369 (s), 1201 (m), 1015 (s), 741 (w) $cm^{-1}$. $C_{32}H_{27}FeN_{11}O_3S_2$ (733.60) calcd. C 52.39, H 3.71, N 21.00 (loss of 1 equiv. of methanol); found C 52.41, H 3.275, N 20.78.

***trans*-[$Fe^{II}(NCS)_2$(DPT)] ($5_\alpha$):** A sample of **5** was isolated by filtration, loaded into a gelatin capsule and heated to 80 °C under high vacuum for 4 h. IR: $\tilde{\nu}$ = 3134 (w), 3067 (w), 2051 (s), 1597 (w), 1553 (m), 1538 (m), 1363 (s), 1281 (m), 1253 (m), 1209 (m), 1014 (w), 766 (w), 754 (w) $cm^{-1}$. $C_{31}H_{21}FeN_{11}OS_2$ (683.55) calcd. C 54.47, H 3.10, N 22.45; found C 55.67, H 3.22, N 22.15.

***trans*-[$Fe^{II}(NCS)_2$(DQT)]·2$CH_2Cl_2$ (6):** DQT (20 mg, 0.038 mmol) was dissolved in dichloromethane (4 mL). Separately, $Fe(ClO_4)_2$ (9.6 mg, 0.038 mmol), NaNCS (6.1 mg, 0.076 mmol) and ascorbic acid (trace) were dissolved in methanol (2.5 mL). A mixture of methanol/dichloromethane (1:1) (8 mL) was layered carefully on top of the dichloromethane/DQT solution, and then the methanolic $Fe(NCS)_2$ solution was layered on top of this. The reaction vial was stoppered, and the solutions were allowed to slowly diffuse together. Over the course of 1 week small yellow block crystals formed, which were collected immediately and washed with dichloromethane (3 × 5 mL) (29.1 mg, 88.5%). IR: $\tilde{\nu}$ = 3267 (br.), 2830 (w), 2057 (s), 1581 (m), 1439 (m), 1363 (s), 1307 (m), 1188 (m), 1156 (m), 912 (w) $cm^{-1}$. $C_{33}H_{25}Cl_4FeN_{11}O_2S_2$ (869.41) calcd. C 45.59, H 2.90, N 17.72; found C 45.33, H 2.95, N 17.49.

***trans*-[$Fe^{II}(NCSe)_2$(DQT)]·$CH_2Cl_2$·$CH_2ClCH_2Cl$ (7):** In methanol (5 mL), $Fe(ClO_4)_2$ (48 mg, 0.189 mmol) and KNCSe (55 mg, 0.379 mmol) were dissolved; the mixture was stirred for 5 min and then allowed to stand at 0 °C for 3 h to precipitate $KClO_4$. After this time, DQT (100 mg, 0.189 mmol) was dissolved in 1,2-dichloroethane/dichloromethane (1:1) (5 mL), and a mixture of methanol/dichloromethane/1,2-dichloroethane (6:1:1) (8 mL) was layered carefully on top of the DQT solution. The methanolic solution of $Fe(NCSe)_2$ was layered on top of this, and the reaction vial was stoppered. The solutions were allowed to slowly diffuse together. Over the course of 1 week small orange block crystals formed, which were collected immediately and washed with 1,2-dichloroethane/dichloromethane (1:1) (3 × 5 mL) (127 mg, 68.8%). IR: $\tilde{\nu}$ = 3262 (br.), 2051 (s), 1600 (s), 1504 (m), 1309 (S), 1187 (m), 1014 (w), 753 (w) $cm^{-1}$. $C_{34}H_{27}Cl_4FeN_{11}O_2Se_2$ calcd. (977.23) C 41.79, H 2.78, N 15.77; found C 42.33, H 2.91, N 15.85. A higher dilution method was used to obtain X-ray quality crystals (see Supporting Information, synthetic details and Figure S40).

***trans*-[$Fe^{II}(NCSe)_2$(DQT)]·1.5$CH_2Cl_2$·0.5$CH_3OH$ (8):** $Fe(ClO_4)_2$ (48 mg, 0.189 mmol) and KNCSe (55 mg, 0.379 mmol) were dissolved in methanol (5 mL), and the mixture was stirred for 5 min and then allowed to stand at 0 °C for 3 h to precipitate $KClO_4$. After this time, DQT (100 mg, 0.189 mmol) was dissolved in dichloromethane (5 mL), and a mixture of methanol/dichloromethane (3:1) (8 mL) was layered carefully on top of the DQT solution. The methanolic solution of $Fe(NCSe)_2$ was layered on top of this, and the reaction vial was stoppered. The solutions were allowed to slowly diffuse together, and over the course of 1 week small orange block crystals formed. These were collected immediately and washed with dichloromethane (3 × 5 mL) (130 mg, 74.7%). IR: $\tilde{\nu}$ = 3261 (br.), 2048 (s), 1583 (s), 1478 (m), 1366 (s), 1241 (m), 1154 (m), 1014 (w), 752 (w) $cm^{-1}$. $C_{33}H_{26}Cl_3FeN_{11}O_{2.5}Se_2$ (936.76) calcd. C 42.31, H 2.80, N 16.45; found C 42.41, H 2.52, N 16.86.

**Mononuclear Complexes**

***trans*-[$Fe^{II}(NCS)_2(DPT)_2$]·2$CH_3OH$ (9):** DPT (20 mg, 0.039 mmol) was dissolved in methanol (1 mL). Separately, $Fe(ClO_4)_2$ (10 mg, 0.039 mmol), NaNCS (6.3 mg, 0.078 mmol) and ascorbic acid (trace) were dissolved in methanol (1 mL). The methanolic DPT solution was placed in one arm of an H-shaped tube (12.5 mL capacity), and the methanolic $Fe(NCS)_2$ solution was placed in the other arm of the same H-shaped tube. Methanol was carefully layered on top of these solutions until the total volume of the H-shaped tube was filled, and the H-shaped tube was stoppered. The reactants were allowed to diffuse together. Over the course of 1 month, yellow plate crystals formed (18 mg, 68.3%). These were not of X-ray diffraction quality. IR: $\tilde{\nu}$ = 3448 (br.), 2829 (w), 2104 (s), 1582 (m), 1535 (s), 1463 (m), 1364 (s), 1202 (m), 1016 (m), 803 (w) $cm^{-1}$. $C_{62}H_{50}FeN_{20}O_4S_2$ (1259.17) calcd. C 59.14, H 4.00, N 22.25; found C 58.80, H 3.77, N 22.54.

***trans*-[$Fe^{II}(NCSe)_2(DPT)_2$]·2$CH_3OH$ (10):** DPT (20 mg, 0.039 mmol) was dissolved in methanol (1 mL). Separately, 10 mg (0.039 mmol) of $Fe(ClO_4)_2$ (10 mg, 0.039 mmol) and KNCSe (11.2 mg, 0.078 mmol) were dissolved in methanol (1 mL), and the mixture was stirred for 5 min and then allowed to stand at 0 °C for 3 h to precipitate $KClO_4$, which was then removed. After this time, the methanolic ligand solution and the methanolic $Fe(NCSe)_2$ solution were transferred into opposite arms of an H-shaped tube (12.5 mL capacity), and methanol was carefully layered on top. The solutions were allowed to slowly diffuse together, and over the course of 1 month, orange plate crystals of high enough quality for single-crystal X-ray diffraction studies formed in quantities too small for bulk analysis. IR, magnetism and microanalytical studies were performed on an orange microcrystalline powder obtained by direct addition of DPT (40 mg, 0.078 mmol), dissolved in methanol (3 mL), to a solution of $Fe(ClO_4)_2$ (20 mg, 0.078 mmol) and KNCSe (23 mg, 0.157 mmol) in methanol (1.5 mL, allowed to stand at 0 °C for 3 h to precipitate $KClO_4$). An orange powder

  

formed immediately, and was washed with fresh methanol (3 × 5 mL) (34.4 mg, 65.1%). IR: $\tilde{\nu}$ = 3460 (w), 3049 (w), 2064 (s), 1580 (m), 1535 (s), 1464 (m), 1364 (s), 1251 (m), 1201 (m), 1089 (w), 907 (w), 744 (w) $cm^{-1}$. $C_{62}H_{50}FeN_{20}O_4Se_2$ (1352.96) calcd. C 55.04, H 3.72, N 20.71; found C 54.30, H 3.25, N 21.34.

**Supporting Information** (see footnote on the first page of this article): $^1H$ and $^{13}C$ NMR spectra for DPPyT, DPT and DQT and further synthetic details for compounds **5**–**10**; tables of structural details and close contacts, Mössbauer plots for **1** and **6**, LIESST kinetics parameters for $\mathbf{1_\beta}$ and $\mathbf{5_\beta}$, special refinement details for single-crystal X-ray and powder diffraction experiments, crystallographic data and parameters for all structures, and full, labeled asymmetric unit pictures for all crystallographic data; thermograms for **7**.

## Acknowledgments

This work was supported by an Australian Research Council (ARC) Discovery Grant to K. S. M. Part of this research was undertaken at the MX1 beamline of the Australian Synchrotron, Victoria, Australia. The authors would like to thank Dr. Rachel Williams from the MX1 beamline at the Australian Synchrotron for her excellent help. Dr. Kia Wallwork and Dr. Qinfen Gu of the Powder Diffraction Beamline at the Australian Synchrotron are thanked for their excellent help with powder diffraction studies. The authors would also like to thank the Aquitaine Region for supporting the development of the international platform for photomagnetism. Valuable discussions with Professor Cameron Kepert are gratefully acknowledged.

[1] P. Gütlich, H. A. Goodwin, *Top. Curr. Chem.* **2004**, *233*, 1–47 and references cited therein. For other reviews, see: P. Gamez, J. S. Costa, M. Quesada, G. Aromi, *Dalton Trans.* **2009**, 7845–7853; A. B. Gaspar, M. Seredyuk, P. Gütlich, *J. Mol. Struct.* **2009**, 9–19.
[2] K. S. Murray, *Eur. J. Inorg. Chem.* **2008**, 3101–3121.
[3] See, for example: M. B. Duriska, S. M. Neville, B. Moubaraki, J. D. Cashion, G. J. Halder, K. W. Chapman, C. Balde, J.-F. Létard, K. S. Murray, C. J. Kepert, S. R. Batten, *Angew. Chem.* **2009**, *121*, 2587; *Angew. Chem. Int. Ed.* **2009**, *48*, 2549–2552; Y. Bodenthin, G. Schwarz, Z. Tomcowicz, T. Geue, W. Haase, U. Pietsch, D. G. Kurth, *J. Am. Chem. Soc.* **2009**, *131*, 2934–2941.
[4] See, for example: J. Kröber, J.-P. Audière, R. Claude, E. Codjovi, O. Kahn, J. G. Haasnoot, F. Grolière, C. Jay, A. Bousseksou, J. Linarès, F. Varret, A. Gonthier-Vassal, *Chem. Mater.* **1994**, *6*, 1404–1412.
[5] L. Salmon, A. Bousseksou, B. Donnadieu, J.-P. Tuchagues, *Inorg. Chem.* **2005**, *44*, 1763–1773.
[6] See, for example: P. D. Southon, L. Liu, E. A. Fellows, D. J. Price, G. J. Halder, K. W. Chapman, B. Moubaraki, K. S. Murray, J.-F. Létard, C. J. Kepert, *J. Am. Chem. Soc.* **2009**, *131*, 10998–11009; M. Seredyuk, A. B. Gaspar, M. C. Muñoz, M. Verdaguer, F. Villain, P. Gütlich, *Eur. J. Inorg. Chem.* **2007**, 4481–4491.
[7] M. Hostettler, K. W. Törnroos, D. Chernyshov, B. Vangdal, H.-B. Bürgi, *Angew. Chem.* **2004**, *116*, 4689; *Angew. Chem. Int. Ed.* **2004**, *43*, 4589–4594.
[8] M. Kepenekian, B. Le Guennic, V. Robert, *Phys. Rev. B* **2009**, *79*, 094428/1–5.
[9] M. Kepenekian, B. Le Guennic, V. Robert, *J. Am. Chem. Soc.* **2009**, *131*, 11498–11502.
[10] S. M. Neville, G. J. Halder, K. W. Chapman, M. B. Duriska, B. Moubaraki, K. S. Murray, C. J. Kepert, *J. Am. Chem. Soc.* **2009**, *131*, 12106–12108.
[11] O. Kahn, C. J. Martinez, *Science* **1998**, *279*, 44–48; see also: J.-F. Létard, P. Guionneau, L. Goux-Capes, *Top. Curr. Chem.* **2004**, 221–249.
[12] J.-F. Létard, *J. Mater. Chem.* **2006**, *16*, 2550–2559.
[13] S. M. Neville, B. A. Leita, D. A. Offerman, M. B. Duriska, B. Moubaraki, K. W. Chapman, G. J. Halder, K. S. Murray, *Eur. J. Inorg. Chem.* **2007**, 1073–1085.
[14] S. M. Neville, B. A. Leita, G. J. Halder, C. J. Kepert, B. Moubaraki, J.-F. Létard, K. S. Murray, *Chem. Eur. J.* **2008**, *14*, 10123–10133.
[15] M. Quesada, V. A. Pena-O'Shea, G. Aromi, S. Geremia, C. Massera, O. Roubeau, P. Gamez, J. Reedijk, *Adv. Mater.* **2007**, *19*, 1397–1402.
[16] S. Bonnet, M. A. Siegler, J. S. Costa, G. Molnár, A. Bousseksou, A. L. Spek, P. Gamez, J. Reedijk, *Chem. Commun.* **2008**, 5619–5621.
[17] M. Nihei, L. Han, H. Oshio, *J. Am. Chem. Soc.* **2007**, *129*, 5312–5313.
[18] B. Li, R.-J. Wei, J. Tao, R.-B. Huang, L.-S. Zheng, Z. Zheng, *J. Am. Chem. Soc.* **2010**, *132*, 1558–1566.
[19] V. Niel, A. L. Thompson, M. C. Muñoz, A. Galet, A. E. Goeta, J. A. Real, *Angew. Chem.* **2003**, *115*, 3890; *Angew. Chem. Int. Ed.* **2003**, *42*, 3760–3763.
[20] P. D. Southon, L. Liu, E. A. Fellows, D. J. Price, G. J. Halder, K. W. Chapman, B. Moubaraki, K. S. Murray, J.-F. Létard, C. J. Kepert, *J. Am. Chem. Soc.* **2009**, *131*, 10998–11009.
[21] M. Ohba, K. Yoneda, G. Agusti, M. C. Muñoz, A. B. Gaspar, J. A. Real, M. Yamasaki, H. Ando, Y. Nakao, S. Sakaki, S. Kitagawa, *Angew. Chem.* **2009**, *121*, 4861; *Angew. Chem. Int. Ed.* **2009**, *48*, 4767–4771.
[22] B. Weber, E. S. Kaps, C. Desplanches, J.-F. Létard, *Eur. J. Inorg. Chem.* **2008**, 2963–2966.
[23] P. de Hoog, P. Gamez, W. L. Driessen, J. Reedijk, *Tetrahedron Lett.* **2002**, *43*, 6783–6786.
[24] B. N. Figgis, *Ligand Field Theory and its Applications*, Wiley-VCH, Weinheim, **1999**.
[25] M. Marchivie, P. Guionneau, J.-F. Létard, D. Chasseau, *Acta Crystallogr., Sect. B* **2005**, *61*, 25–28.
[26] M. Quesada, M. Monrabal, G. Aromí, V. A. de la Peña-O-Shea, M. Gich, E. Molins, O. Roubeau, S. J. Teat, E. J. MacLean, P. Gamez, J. Reedijk, *J. Mater. Chem.* **2006**, *16*, 2669–2676.
[27] A. Galet, A. B. Gaspar, M. C. Muñoz, G. Levchenko, J. A. Real, *Inorg. Chem.* **2006**, *45*, 9670–9679.
[28] P. Guionneau, M. Marchivie, G. Bravic, J.-F. Létard, D. Chasseau, *Top. Curr. Chem.* **2004**, *234*, 97–128.
[29] B. A. Hunter, C. J. Howard, in *A Computer Program for Rietveld Analysis of X-ray and Neutron Powder Diffraction Patterns*, Lucas Heights Research Laboratories, Sydney, Australia, **1998**, p. 1.
[30] See, for example: C.-F. Sheu, S.-Z. Chen, S.-C. Wang, G.-H. Lee, Y.-H. Liu, Y. Wang, *Chem. Commun.* **2009**, 7512–7514.
[31] P. Guionneau, M. Marchivie, G. Bravic, J.-F. Létard, D. Chasseau, *J. Mater. Chem.* **2002**, *12*, 2546–2551.
[32] See, for example D. Glijer, J. Hébert, E. Trzop, E. Collet, L. Toupet, G. S. Matouzenko, H. Z. Lazar, J.-F. Létard, S. Koshihara, M. Buron-Le Cointe, *Phys. Rev. B* **2008**, *78*, 134112.
[33] J. A. Real, B. Gallois, T. Granier, F. Suez-Panamá, J. Zarembowitch, *Inorg. Chem.* **1992**, *31*, 4972–4979.
[34] P. J. van Koningsbruggen, Y. Garcia, O. Kahn, L. Fournés, H. Kooijman, A. L. Spek, J. G. Haasnoot, J. Moscovici, K. Provost, A. Michalowicz, F. Renz, P. Gütlich, *Inorg. Chem.* **2000**, *39*, 1891–1900.
[35] T. J. Mooibroek, P. Gamez, *Inorg. Chim. Acta* **2007**, *360*, 381–404.
[36] J. J. M. Amoore, S. M. Neville, B. Moubaraki, S. S. Iremonger, K. S. Murray, J.-F. Létard, C. J. Kepert, *Chem. Eur. J.* **2010**, *16*, 1973–1982.
[37] C. P. Slichter, H. G. Drickamer, *J. Chem. Phys.* **1972**, *56*, 2142–2160.

  

[38] H. Spiering, *Top. Curr. Chem.* **2004**, *235*, 171–195.
[39] P. Guionneau, J.-F. Létard, D. S. Yufit, D. Chasseau, G. Bravic, A. E. Goeta, J. A. K. Howard, O. Kahn, *J. Mater. Chem.* **1999**, *9*, 985–994.
[40] C. J. Kepert, personnel communication, **2010**.
[41] S. Pillet, V. Legrand, H.-P. Weber, M. Souhassou, J.-F. Létard, P. Guionneau, C. Lecomte, *Z. Kristallogr.* **2008**, *223*, 235–249.
[42] V. Legrand, S. Pillet, M. Souhassou, N. Lugan, C. Lecomte, *J. Am. Chem. Soc.* **2006**, *128*, 13921–13931.
[43] *APEX2 Software Package*, v. 2-01, Bruker AXS, Inc., Madison, WI, **2005**.
[44] *SHELXL97 – Program for crystal structural solution and refinement*, Bruker Analytical Instruments, Inc., Madison, Wisconsin, USA, **1997**; L. J. Barbour, *X-SEED*, University of Stellenbosch, South Africa, **1999**.
[45] T. M. McPhillips, S. E. McPhillips, H. J. Chiu, A. E. Cohen, A. M. Deacon, P. J. Ellis, E. Garman, A. Gonzalez, N. K. Sauter, R. P. Phizackerley, S. M. Soltis, P. Kuhn, *J. Synchrotron Radiat.* **2002**, *9*, 401–406.
[46] W. J. Kabsch, *Appl. Crystallogr.* **1993**, *26*, 795–800.
[47] P. J. Chupas, M. F. Ciraolo, J. C. Hanson, C. P. Grey, *J. Am. Chem. Soc.* **2001**, *123*, 1694–1702.
[48] A. P. Hammersley, *ESRF Internal Report* **1997**, ESRF97HA02T.
[49] A. P. Hammersley, S. O. Svensson, M. Hanfland, A. N. Fitch, D. Hausermann, *High Pressure Res.* **1996**, *14*, 235–248.
[50] A. C. Larson, R. B. V. Dreele, "General Structure Analysis System (GSAS)", *Los Alamos National Laboratory Report* **2000**, LAUR 86-748.

Received: August 14, 2010
Published Online: February 7, 2011

  